Steel and Composite Structures, *Vol. 35, No. 2 (2020) 215-235*
DOI: https://doi.org/10.12989/scs.2020.35.2.215

Effect of crack location on buckling analysis and SIF of cracked plates under tension

Parham Memarzadeh*[1], Sayedmohammad Mousavian[1], Mohammad Hosseini Ghehi[1] and Tadeh Zirakian[2]

[1]*Department of Civil Engineering, Najafabad Branch, Islamic Azad University, Najafabad, Iran*
[2]*Department of Civil Engineering and Construction Management, California State University, Northridge, CA, USA*

(*Received October 13, 2019, Revised February 13, 2020, Accepted February 17, 2020*)

Abstract. Cracks and defects may occur anywhere in a plate under tension. Cracks can affect the buckling stability performance and even the failure mode of the plate. A search of the literature reveals that the reported research has mostly focused on the study of plates with central and small cracks. Considering the effectiveness of cracks on the buckling behavior of plates, this study intends to investigate the effects of some key parameters, i.e., crack size and location as well as the plate aspect ratio and support conditions, on the buckling behavior, stress intensity factor (SIF), and the failure mode (buckling or fracture) in cracked plates under tension. To this end, a sophisticated mathematical code was developed using MATLAB in the frame-work of extended finite element method (XFEM) in order to analyze the buckling stability and collapse of numerous plate models. The results and findings of this research endeavor show that, in addition to the plate aspect ratio and support conditions, careful consideration of the crack location and size can be quite effective in buckling behavior assessment and failure mode prediction as well as SIF evaluation of the cracked plates subjected to tensile loading.

Keywords: cracked plates; tensile loading; buckling; stress intensity factor; extended finite element method

1. Introduction

Plates or sheets are among the common structural components used in aerospace, ships, offshore and other complex industries. Thin plates can contain different types of defects such as cracks created due to imperfection, fatigue, impact, corrosion, and so on. Study of the cracked plates under different loads is required to assess an acceptable level of structural safety. Buckling is a phenomenon which can more likely occur in thin plates especially when some imperfections as cracks exist. In addition to compressive loads which can result in plate buckling, cracked plates may also buckle under tensile loads due to formation of compression fields in areas around the crack. Buckling may affect the loading capacity of plates; such that according to Seif and Kabir (2017), the buckling of tension cracked plates can reduce the fracture capacity and the fatigue life by 35% and 59%, respectively.

In the past decade, some researchers have studied buckling of perforated and cracked plates (Serror *et al.* 2016, Lei *et al*. 2018, Zakeri *et al.* 2018, Saberi *et al.* 2019). The obtained results indicate that the type of boundary conditions has considerable effect on compressive buckling stress, even more than presence of the crack; while, the tensile buckling stress is almost independent of the boundary conditions and is significantly affected by the crack length (Brighenti 2005). In the case of plates with all simply supported or clamped edges, the effect of crack is the increase of compressive buckling stress up to 10% compared to un-cracked plate (Brighenti 2005, Brighenti 2009); while, the opposite happens for plates with two free opposite edges parallel to the loading direction (Pan *et al*. 2013). Furthermore, the tensile buckling stress is higher than corresponding compressive one, and tends to increase rapidly by reducing the crack length (Brighenti 2005, Amiri Rad *et al*. 2014). In these results, the crack edges are perpendicular to loading direction. Study of compressive buckling of plates with cracks whose edges are parallel to crack clarifies that the above mentioned results cannot be extended to these cases (Pan *et al*. 2013). The effect of tensile load on buckling of cracked plates was investigated in another study (Seifi and Kabiri 2013). It was found that the tensile load increases the buckling load, while the compression decreases it. The perforated and cracked plates under shear loadings have also been studied by some researchers (Brighenti *et al*. 2011, Cheng *et al.* 2012, Nasirmanesh *et al*. 2015, Liu *et al*. 2015).

Most research ever done regarding buckling of cracked plates is limited to the study of plates with either central or edged cracks. While cracks may occur at any location in the plate, the study of the effect of crack position on critical buckling load and probable mode of fracture is of utmost importance for engineers from design perspective. From the few research works reported in this respect, some studies, i.e., (Khedmati *et al*. 2009, Yin *et al*. 2016, Yu *et al*. 2016, Saberi *et al*. 2019), are considered herein. Khedmati *et al*. (2009) and Saberi *et al*. (2019) performed finite element studies on the buckling strength of cracked plates under compression. The considered plate was assumed to be simply supported and also limited to the cracks with lengths no longer than half the width of plate; in addition, the

*Corresponding author, Ph.D.
E-mail: p-memar@iaun.ac.ir

ISSN: 1229-9367 (Print), 1598-6233 (Online)

location of cracks was chosen such that the crack centers were in a distance from the center of plate in the direction perpendicular to loading edges. It was found that the plate aspect ratio is an effective parameter on buckling behavior; also, the crack size and location may have major effects on buckling mode (Brighenti 2005).

This paper aims to investigate the buckling behavior of non-centrally cracked plates under tensile loading. Parameters examined in this study are the crack length (including short to long cracks), plate aspect ratio (0.5, 1.0, and 2.0), plate support conditions, and location of the cracks with eccentricities in directions parallel or perpendicular to loading edges. Also, the influence of crack location on the stress intensity factor (SIF) is investigated to predict the plate failure (fracture or buckling) mode. To this end, Mindlin's first-order shear deformation theory (FSDT) of plates is used in the frame-work of extended finite element method (XFEM) (Khoei 2014, Mohammadi 2008) to analyze both in-plane and eigen-buckling equations. To verify the validity of models, the results for buckling and SIF are compared with both analytical and numerical solutions available in the literature. XFEM is able to model singularity of the stress field near the crack tips and also to capture strong discontinuities in the forms of jumps in displacement field across the crack faces. According to Nasirmanesh *et al*. (2015), this ability of XFEM leads to an increase in accuracy of results compared to the conventional finite element method (FEM) used in previous research endeavors (Brighenti 2005 and 2009, Seifi and Kabiri 2013). It is noted that XFEM was used by some researchers (Amiri Rad *et al*. 2014, Nasirmanesh *et al*. 2015, Liu *et al*. 2015) to analysis of buckling of cracked plates. Moreover, Rayleigh-Ritz method has also been previously (Pan *et al*. 2013, Satish Kumar and Paik 2014) used for the analysis of such plates.

The novelty and contribution of this research endeavor is that it considers large-size cracks, while previous research has focused on relatively small-size cracks. In fact, this study aims to demonstrate the different performances of plates with large cracks in terms of changing the buckling mode to semi-global instability and also the significant effectiveness of plate boundary conditions on the buckling coefficient. Furthermore, the effects of crack location on the buckling and collapse behaviors of tensioned plates are investigated in this paper.

2. Basic formulation

In this study, the element formulation is based on Mindlin-Reissner theory of plates which includes transverse shear deformations. The linear buckling equations are solved by XFEM. 4-noded quadrilateral plate elements, as illustrated in Fig. 1, are used here to discretize the geometry of the plate. Fig. 1 gives geometric of the cracked 4-noded plate element.

2.1 Kinematics

The general form of the XFEM approximation for the displacement field of any point $\mathbf{x}$ is defined as the conventional finite element approximation in addition to terms added in order to consider the crack face discontinuity and the stress singularity at crack tips. Including the transverse shear deformation effects, the XFEM approximation field in modeling of crack interface for an isotropic flat plate can be written by applying some simplifications on the case of general shell element (Nasirmanesh and Mohammadi 2015) as

$$u = \sum_{i\in\mathcal{N}_{fem}} N_i \bar{u}_i^{fem} + \sum_{j\in} N_j \bar{u}_j^{dis}(H(\mathbf{x}) - H(\mathbf{x}_j)) + \sum_{k\in} N_k \sum_{l=1}^{4} \bar{u}_{kl}^{tip}(F_l(\mathbf{x}) - F_l(\mathbf{x}_j)) \quad (1)$$

$$v = \sum_{i\in} N_i \bar{v}_i^{fem} + \sum_{j\in} N_j \bar{v}_j^{dis}(H(\mathbf{x}) - H(\mathbf{x}_j)) + \sum_{k\in} N_k \sum_{l=1}^{4} \bar{v}_{kl}^{tip}(F_l(\mathbf{x}) - F_l(\mathbf{x}_k)) \quad (2)$$

$$w = \sum_{i\in} N_i \bar{w}_i^{fem} + \sum_{j\in} N_j \bar{w}_j^{dis}(H(\mathbf{x}) - H(\mathbf{x}_j)) + \sum_{k\in} N_k \bar{w}_k^{tip}(G(\mathbf{x}) - G(\mathbf{x}_k)) \quad (3)$$

where u, v and w are the displacement components in x, y and z directions, respectively; N_i are conventional shape functions; The superscripts: *fem*, *dis* and *tip* denote that superscripted variables are associated with conventional FEM, discontinuity across the crack face and singularity around the crack tip, respectively; $\mathcal{N}_{fem}$ is the set of all nodal points of element; as well as $\mathcal{N}_{dis}$ and $\mathcal{N}_{tip}$ are the sets of nodes that contain the crack face and crack tip in the support of shape functions enriched by Heaviside ($H(\mathbf{x})$) and asymptotic ($F(\mathbf{x})$ or $G(\mathbf{x})$) functions, respectively; $\overline{u_i}^{\blacksquare}$ and $\overline{v_i}^{\blacksquare}$ and $\overline{w_i}^{\blacksquare}$ are defined as below

$$\overline{u}_{\square}^{\blacksquare} = u_{\square}^{\blacksquare} + z\ \beta_{\square}^{\blacksquare}\ ,\ \overline{v}_{\square}^{\blacksquare} = v_{\square}^{\blacksquare} - z\ \alpha_{\square}^{\blacksquare} \text{ and } \overline{w}_{\square}^{\blacksquare} = w_{\square}^{\blacksquare} \quad (4)$$

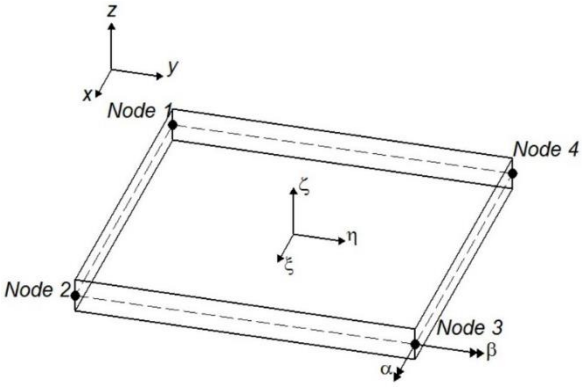

Fig. 1 Geometry of the 4-noded cracked plate element

where ■ is a superscript which can be replaced by one of the previously defined superscripts: *fem*, *dis* or *tip*; □ is a subscript which indicates that the subscribed variable belongs to nodal point □; whereas, in which case (■ = *tip*) the subscript □ consists of two indices as *kl* in Eqs. (1) and (2). The first index, *k*, is related to the number of nodes and the second one, *l*, corresponds to the asymptotic function $F_l(\mathbf{x})$. $(u_i\ , v_i\ )$ and $(\alpha_i^{\square}, \beta_i^{\square})$ are the nodal degrees of freedom corresponding to the displacements and rotations at node *i* with respect to *x* and *y* directions, respectively. $\mathbf{u}^{\blacksquare}$ is defined as

$$\mathbf{u}^{\blacksquare} = \{u_{\square}^{\blacksquare}, v_{\square}^{\blacksquare}, w_{\square}^{\blacksquare}, \alpha_{\square}^{\blacksquare}, \beta_{\square}^{\blacksquare}\}^T \tag{5}$$

where, ■ and □ are the previously defined superscripts and subscripts, respectively; $\mathbf{u}^{fem}$ is the standard vector of unknowns; while, $\mathbf{u}^{dis}$ and $\mathbf{u}^{tip}$ are enrichment vectors of degrees of freedom added to consider the discontinuity of crack face and stress singularity at crack tip, respectively. The Heaviside function at point **x** is defined as

$$H(\mathbf{x}) = \begin{cases} +1 & \mathbf{x}\ above\ the\ crack \\ -1 & \mathbf{x}\ under\ the\ crack \end{cases} \tag{6}$$

The in-plane tip enrichment functions are derived according to the asymptotic solution for displacements around a finite line crack in an infinite plate under in-plane tension and shear (Williams 1957). The mentioned displacements are expressed as below (Broek 1974)

$$\begin{Bmatrix} u^{tip} \\ v^{tip} \end{Bmatrix} = \begin{Bmatrix} \frac{K_I(1+\nu)}{E}\sqrt{\frac{r}{2\pi}}\cos\frac{\theta}{2}\left(\vartheta - 1 + 2\sin^2\frac{\theta}{2}\right) \\ \frac{K_I(1+\nu)}{E}\sqrt{\frac{r}{2\pi}}\sin\frac{\theta}{2}\left(\vartheta + 1 - 2\cos^2\frac{\theta}{2}\right) \end{Bmatrix} + \begin{Bmatrix} \frac{K_{II}(1+\nu)}{E}\sqrt{\frac{r}{2\pi}}\sin\frac{\theta}{2}\left(\vartheta + 1 + 2\cos^2\frac{\theta}{2}\right) \\ \frac{K_{II}(1+\nu)}{E}\sqrt{\frac{r}{2\pi}}\cos\frac{\theta}{2}\left(\vartheta - 1 - 2\sin^2\frac{\theta}{2}\right) \end{Bmatrix} \tag{7}$$

where (r, θ) are the polar coordinates of the local coordinate system defined with an origin at the tip of crack and with basis vectors defined by the unit vector's tangent and normal to the crack at the crack tip (Fig. 2(a)); K_I and K_{II} are the modes I and II membrane stress intensity factors (SIFs); and $\vartheta = (3-\nu)/(1+\nu)$ for plane stress; where, E and ν are the elastic modulus and Poisson's ratio, respectively. Thus, four in-plane enrichments based on Eq. (7) are defined for two-dimensional isotropic media as

$$F(r,\theta) = \left\{\sqrt{r}\sin\frac{\theta}{2}, \sqrt{r}\cos\frac{\theta}{2}, \sqrt{r}\sin\frac{\theta}{2}\sin\theta, \sqrt{r}\sin\frac{\theta}{2}\cos\theta\right\}^T \tag{8}$$

Also, the out-of-plane and rotation enrichment functions can be derived according to the asymptotic solution for out-of-plane displacement and rotations. The mentioned displacement and rotations based on the Mindlin–Reissner theory for a shear-deformable plate under out of plane loading are as below (Delbow 2000)

$$\begin{aligned} w^{tip} &= \frac{6\sqrt{2r}}{5\mu t}K_{b3}\sin\frac{\theta}{2} \\ &+ \frac{6\sqrt{2}r^{\frac{3}{2}}K_{b1}}{Et^3}\left[\frac{1}{3}(7+\nu)\cos\frac{3\theta}{2} - (1-\nu)\cos\frac{\theta}{2}\right] \\ &+ \frac{6\sqrt{2}r^{\frac{3}{2}}K_{b2}}{Et^3}\left[-\frac{1}{3}(5+3\nu)\sin\frac{3\theta}{2} + (1-\nu)\sin\frac{\theta}{2}\right] \end{aligned} \tag{9}$$

$$\begin{aligned} \alpha^{tip} &= \frac{6\sqrt{2r}K_{b1}}{Et^3}\cos\frac{\theta}{2}[4-(1+\nu)(1+\cos\theta)] \\ &+ \frac{6\sqrt{2r}K_{b2}}{Et^3}\sin\frac{\theta}{2}[4+(1+\nu)(1+\cos\theta)] \\ &+ \frac{6\sqrt{2}r^{\frac{3}{2}}K_{b3}}{Et^3}\left(\frac{18}{15}\right)\left[-\sin\frac{\theta}{2} - (1+3\nu)\cos\frac{\theta}{2}\sin\theta\right] \end{aligned} \tag{10}$$

$$\begin{aligned} \beta^{tip} &= \frac{6\sqrt{2r}K_{b1}}{Et^3}\sin\frac{\theta}{2}\left[-4-2(1+\nu)\cos^2\frac{\theta}{2}\right] \\ &+ \frac{6\sqrt{2r}K_{b2}}{Et^3}\cos\frac{\theta}{2}\left[(1-\nu)+(1+\nu)\sin^2\frac{\theta}{2}\right] \\ &+ \frac{6\sqrt{2}r^{\frac{3}{2}}K_{b3}}{Et^3}\left(\frac{18}{15}\right)\cos\frac{\theta}{2}[1 + (1+3\nu)\cos\theta] \end{aligned} \tag{11}$$

where, t is the plate thickness; μ is shear modulus; and K_{b1}, K_{b2}, K_{b3} are the bending stress intensity factors. Then, according to Eqs. (9)-(11), out-of-plane and rotation enrichments are defined as Eqs. (12) and (13), respectively

$$G(r,\theta) = \left\{\begin{matrix} \sqrt{r}\sin\frac{\theta}{2}, r^{\frac{3}{2}}\sin\frac{\theta}{2}, r^{\frac{3}{2}}\cos\frac{\theta}{2}, r^{\frac{3}{2}}\sin\frac{3\theta}{2}, \\ r^{3/2}\cos\frac{3\theta}{2} \end{matrix}\right\}^T \tag{12}$$

$$R(r,\theta) = \left\{\sqrt{r}\sin\frac{\theta}{2}, \sqrt{r}\cos\frac{\theta}{2}, \sqrt{r}\sin\frac{\theta}{2}\sin\theta, \sqrt{r}\sin\frac{\theta}{2}\cos\theta\right\}^T \tag{13}$$

It should be noted that, these rotation enrichments (R) are similar to in-plane enrichments (F); therefore, Eqs. (1) and (2) are the simplified equations assuming equality of R and F. By considering only the terms those are proportional to $\sqrt{r}$ for w^{tip}, the out of plane enrichments are simplified to (Nasirmanesh and Mohammadi 2015, Bayesteh and Mohammadi 2011)

$$G(r,\theta) = \sqrt{r}\sin\frac{\theta}{2} \tag{14}$$

ε_{ij}^L and ε_{ij}^{NL} components of the respective linear and non-linear parts of Green-Lagrange strain tensor can be written in terms of displacement derivatives, as below

$$\varepsilon_{ij}^L = \frac{1}{2}\left(u_{i,j} + u_{j,i}\right) \qquad \text{and} \tag{15}$$

$$\varepsilon_{ij}^{NL} = \frac{1}{2}\sum_{k=1}^{3} u_{k,i}u_{k,j} \ (i,j \ = 1,2,3)$$

where, the indices 1, 2 and 3 are corresponding to *x*, *y* and *z* directions, respectively. Further, a subscript with comma denotes the coordinate partial derivative with respect to the geometric variables.

2.2 Buckling analysis

Assuming no in-plane motion of mid-plane at the moment of buckling, the terms representing the in-plane motions, i.e., $u_{\square}^{\blacksquare}$ and $v_{\square}^{\blacksquare}$, can be removed from Eqs. (4) and (5); therefore, Eq. (5) is simplified to

$$\mathbf{w}^{\blacksquare} = \{w_{\square}^{\blacksquare}, \alpha_{\square}^{\blacksquare}, \beta_{\square}^{\blacksquare}\}^T \tag{16}$$

where, $\mathbf{w}^{\blacksquare}$ is the vector of out-of-plane degrees of freedom. In the case of buckling, the expression for the principle of virtual work is

$$\int_V \delta\boldsymbol{\varepsilon}^{L^T}\mathbf{D}\ \boldsymbol{\varepsilon}^{L}\ dV + \int_V \delta\boldsymbol{\varepsilon}^{NL^T}\hat{\mathbf{S}}\ dV = 0 \tag{17}$$

in which, δ denotes virtual quantities. Given that the state of stress in the plate corresponding to the plane stress, $\delta\varepsilon_{zz}^{L}$, does not contribute to total virtual work; therefore, the linear ($\boldsymbol{\varepsilon}^{L}$) and non-linear ($\boldsymbol{\varepsilon}^{NL}$) strain vectors in Eq. (17) can be written as

$$\boldsymbol{\varepsilon}^{L} = \left\{\varepsilon_{xx}^{L}, \varepsilon_{yy}^{L}, \varepsilon_{xy}^{L}, \varepsilon_{yz}^{L}, \varepsilon_{zx}^{L}\right\}^T \quad \text{and} \quad \boldsymbol{\varepsilon}^{NL} = \left\{\varepsilon_{xx}^{NL}, \varepsilon_{yy}^{NL}, \varepsilon_{xy}^{NL}, \varepsilon_{yz}^{NL}, \varepsilon_{zx}^{NL}\right\}^T \tag{18}$$

which can be obtained from Eq. (15). $\mathbf{D}$ is the tensor of material properties

$$\mathbf{D} = \frac{E}{(1-\nu^2)}\begin{bmatrix} 1 & \nu & 0 & 0 & 0 \\ \nu & 1 & 0 & 0 & 0 \\ 0 & 0 & (1-\nu)/2 & 0 & 0 \\ 0 & 0 & 0 & \kappa(1-\nu)/2 & 0 \\ 0 & 0 & 0 & 0 & \kappa(1-\nu)/2 \end{bmatrix} \tag{19}$$

where, E and ν are the elastic modulus and Poisson's ratio, respectively; also, κ is a constant to account for actual non-uniformity of the shearing stresses (which is usually taken as 5/6) (Bathe 1996). Corresponding to the strain vector, the initial stress vector, $\hat{\mathbf{S}}$, is written as below

$$\hat{\mathbf{S}} = \{S_{xx}, S_{yy}, S_{xy}, S_{yz}, S_{zx}\}^T \tag{20}$$

whereas, its components are second Piola-Kirchhoff stresses obtained by pre-buckling in-plane analysis of the cracked plate described in section 2.3 Substituting from Eqs. (18)-(20) into Eq. (17), the following eigenvalue equation is obtained

$$(\mathbf{K}_S + \lambda\ \mathbf{K}_G)\{\mathbf{w}\} = 0 \tag{21}$$

where, λ represents eigenvalue and $\mathbf{w}$ is eigenvector

$$\mathbf{w} = \{(\mathbf{w}^{fem})^T, (\mathbf{w}^{dis})^T, (\mathbf{w}^{tip}|_1)^T, (\mathbf{w}^{tip}|_2)^T, (\mathbf{w}^{tip}|_3)^T, (\mathbf{w}^{tip}|_4)^T\}^T \tag{22}$$

where, $\mathbf{w}^{\blacksquare}$ has been defined in Eq. (16) and $\mathbf{w}^{tip}|_l$ means $\mathbf{w}^{tip}$ corresponding to $F(\mathbf{x}) = F_l(\mathbf{x})$. $\mathbf{K}_S$ and $\mathbf{K}_G$ are the standard and geometric stiffness matrices, respectively

$$\mathbf{K}_S = \int_V \mathbf{B}_S^T\mathbf{D}\,\mathbf{B}_S dV \quad \text{and} \quad \mathbf{K}_G = \int_V \mathbf{B}_G^T\mathbf{S}\,\mathbf{B}_G dV \tag{23}$$

in which

$$\mathbf{B}_S = \left[\mathbf{B}_S^{fem} \quad \mathbf{B}_S^{dis} \quad \mathbf{B}_S^{tip}|_1 \quad \mathbf{B}_S^{tip}|_2 \quad \mathbf{B}_S^{tip}|_3 \quad \mathbf{B}_S^{tip}|_4\right]$$
$$\mathbf{B}_G = \left[\mathbf{B}_G^{fem} \quad \mathbf{B}_G^{dis} \quad \mathbf{B}_G^{tip}|_1 \quad \mathbf{B}_G^{tip}|_2 \quad \mathbf{B}_G^{tip}|_3 \quad \mathbf{B}_G^{tip}|_4\right] \tag{24}$$

In Eq. (24), $\mathbf{B}_S^{tip}|_l$ and $\mathbf{B}_G^{tip}|_l$ indicate that the respective $\mathbf{B}_S^{tip}$ and $\mathbf{B}_S^{tip}$ correspond to $F(\mathbf{x}) = F_l(\mathbf{x})$. By applying some simplifications, $\mathbf{B}_S^{\blacksquare}$ and $\mathbf{B}_G^{\blacksquare}$ can be obtained for plate elements (Cook 2007)

$$\mathbf{B}_S^{\blacksquare} = \begin{bmatrix} 0 & -zN_{i,x}^{\blacksquare} & 0 \\ 0 & 0 & zN_{i,y}^{\blacksquare} \\ 0 & -zN_{i,y}^{\blacksquare} & zN_{i,x}^{\blacksquare} \\ N_{i,y}^{\blacksquare} & 0 & N_i^{\blacksquare} \\ N_{i,x}^{\blacksquare} & -N_i^{\blacksquare} & 0 \end{bmatrix}$$

and

$$\mathbf{B}_G^{\blacksquare} = \begin{bmatrix} 0 & -zN_{i,x}^{\blacksquare} & 0 \\ 0 & 0 & zN_{i,y}^{\blacksquare} \\ 0 & -N_i^{\blacksquare} & N_i^{\blacksquare} \\ 0 & -zN_{i,x}^{\blacksquare} & 0 \\ 0 & 0 & zN_{i,y}^{\blacksquare} \\ 0 & -N_i^{\blacksquare} & N_i^{\blacksquare} \\ N_{i,x}^{\blacksquare} & -zN_{i,x}^{\blacksquare} & 0 \\ N_{i,y}^{\blacksquare} & 0 & zN_{i,y}^{\blacksquare} \\ 0 & -N_i^{\blacksquare} & N_i^{\blacksquare} \end{bmatrix} \tag{25}$$

where, superscript ■ was previously defined and can be replaced by one of the superscripts: *fem*, *dis* or *tip*. $N_i^{\blacksquare}$ is defined as below

$$N_i^{fem} = N_i, \quad N_i^{dis} = N_i\ (H(\mathbf{x}) - H(\mathbf{x}_i)) \quad \text{and} \quad N_i^{tip} = N_i\ (F(\mathbf{x}) - F_l(\mathbf{x}_i)) \tag{26}$$

Stress matrix ($\mathbf{S}$) in Eq. (23) is written as

$$\mathbf{S} = \begin{bmatrix} \bar{\mathbf{S}} & 0 & 0 \\ 0 & \bar{\mathbf{S}} & 0 \\ 0 & 0 & \bar{\mathbf{S}} \end{bmatrix} \tag{27}$$

where

$$\bar{\mathbf{S}} = \begin{bmatrix} S_{xx} & S_{xy} & S_{zx} \\ S_{xy} & S_{yy} & S_{yz} \\ S_{zx} & S_{yz} & S_{zz} \end{bmatrix} \tag{28}$$

2.3 Pre-buckling analysis

As seen in Eq. (17), the buckling analysis needs to know about the stress distribution across the plate. Due to the presence of crack, the distribution of stresses in the plate is not uniform; however, the stress distribution can be found through a well-known linear in-plane analysis. Thus, the components S_{zz}, S_{zx} and S_{yz} of $\hat{\mathbf{S}}$ and $\bar{\mathbf{S}}$ in Eqs. (20)-

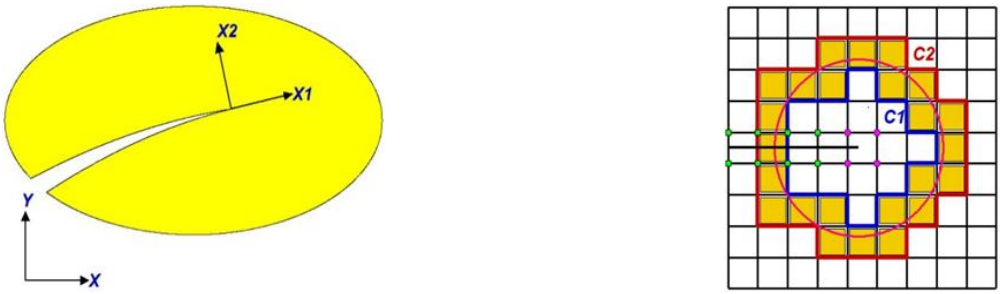

(a) (b)

Fig. 2 (a) Local crack tip and global coordinate systems and (b) J-integral domain selected by virtual circle and bounded by inner and outer contours

(28), respectively, should be equal to zero. XFEM approximation for in-plane analysis of cracked plate is also based on Eqs. (1)-(3). The details of in-plane analysis is not given here for brevity.

2.4 Shear locking

The basic difficulty in formulation of the plate elements in the framework of Mindlin theory is the effect of shear locking. This phenomenon occurs in thin plates and shells due to the prediction of spurious shear stresses that leads to a strong artificial stiffening of the element. Some researchers intended to use 8-noded elements, because these elements in conjunction with reduced integration scheme avoid mesh distortion and shear locking (Nasirmanesh and Mohammadi 2015); however, the use of lower-order elements can save time in numerical simulation calculations of the FEM program.

In this research endeavor, 4-noded elements were used to mesh the plate domain. It is evident that the shear locking effect is more pronounced for low-order elements (Bathe 1996); hence, in order to avoid the shear locking, the selective integration scheme was adopted to numerically evaluate the stiffness matrices in Eq. (23). In the case of selective integration, different strain terms were integrated with different orders of integration (Bathe 1996). In the following, the details of the applied numerical integration technique are presented.

2.5 SIF analysis

For calculating SIF, in-plane results are employed to apply the J-integral technique. In this technique, J-integral is defined as (Khoei 2014):

$$J = \int_A \left(\sigma_{ij}\frac{\partial u_i}{\partial x_1} - \mathcal{W}\delta_{1j}\right)\frac{\partial q}{\partial x_j}dA \tag{29}$$

where, σ_{ij} and u_i are denoting the stress tensor and displacement field in local crack tip coordinate system (x_1,x_2) as shown in Fig. 2(a), respectively; $\mathcal{W}$ is the strain energy density defined as

$$\mathcal{W} = \frac{1}{2}\sigma_{ij}\varepsilon_{ij} \tag{30}$$

with ε_{ij} = strain tensor; ε_{ij}, σ_{ij} and u_i are obtained from XFEM in-plane analysis, and are transferred from the global to local crack tip coordinate system by using an appropriate transformation; δ is the Kronecker delta and q is a weighting function defined over the domain of integration; Such that is equal to unit at the crack tip and vanishes on an outer prescribed contour (*C2* in Fig. 2(b)). A is the J-integral domain for computation of SIF bounded by crack interface, inner and outer contours (*C1* and *C2* in Fig. 2(b), respectively).

In XFEM modeling, the J-integral domain is obtained by assuming a virtual circle with a specific radius around the crack tip, and the integration is performed over the elements crossed by this circle (shaded elements in Fig. 2(b)) (Khoei 2014). The distribution of q can be obtained within an element using the standard FE interpolation as

$$q = \sum_{i\in} N_i q_i \tag{31}$$

where, q_i is the nodal value of q, which is equal to 1.0 if the node is on the inner contour (*C1*, near the crack tip) and is equal to 0 if the node is on the outer contour (*C2*).

The energy release rate ($\mathcal{G}$) for 2D mixed-mode crack problems can be generally defined based on the SIFs of the modes I and II, i.e. K_I and K_{II}, as (Khoei 2014)

$$J \equiv \mathcal{G} = \frac{1}{E'}({K_I}^2 + {K_{II}}^2) \tag{32}$$

In this equation, $E' = E$ for plane stress. By considering two states of a crack body, that is, the true state (1) called by $({u_i}^{(1)}, {\varepsilon_{ij}}^{(1)}, {\sigma_{ij}}^{(1)})$ and an auxiliary state (2) denoted by $({u_i}^{(2)}, {\varepsilon_{ij}}^{(2)}, {\sigma_{ij}}^{(2)})$, the J-integral for the sum of states (1) and (2) can be written according to Eq. (29) and (30) as

$$\begin{aligned} J^{(1+2)} = \int_A \Big(& (\sigma_{ij}{}^{(1)} + \sigma_{ij}{}^{(2)})\frac{\partial}{\partial x_1}(u_i{}^{(1)} + u_i{}^{(2)}) \\ & - \frac{1}{2}(\sigma_{ij}{}^{(1)} + \sigma_{ij}{}^{(2)})(\varepsilon_{ij}{}^{(1)} \\ & + \varepsilon_{ij}{}^{(2)})\delta_{1j}\Big)\frac{\partial q}{\partial x_j}dA \end{aligned} \tag{33}$$

Expanding this expression results in

$$J^{(1+2)} = J^{(1)} + J^{(2)} + I^{(1,2)} \tag{34}$$

where $I^{(1,2)}$ is called the interaction integral for state (1) and (2) defined as

$$I^{(1+2)} = \int_A \left({\sigma_{ij}}^{(1)} \frac{\partial {u_i}^{(2)}}{\partial x_1} + {\sigma_{ij}}^{(2)} \frac{\partial {u_i}^{(1)}}{\partial x_1} - \mathcal{W}^{(1,2)} \delta_{1j} \right) \frac{\partial q}{\partial x_j} dA \quad (35)$$

where $\mathcal{W}^{(1,2)}$ is the interaction strain energy defined by

$$\mathcal{W}^{(1,2)} = {\sigma_{ij}}^{(1)} {\varepsilon_{ij}}^{(2)} = {\sigma_{ij}}^{(2)} {\varepsilon_{ij}}^{(1)} \quad (36)$$

Based on Eq. (32), Eq. (34) can be rewritten as

$$J^{(1+2)} = J^{(1)} + J^{(2)} + \frac{2}{E'} ({K_I}^{(1)} {K_{II}}^{(2)} + {K_I}^{(2)} {K_{II}}^{(1)}) \quad (37)$$

Comparing Eq. (35) with (37), the interaction $I^{(1+2)}$ can be obtained as

$$I^{(1+2)} = \frac{2}{E'} ({K_I}^{(1)} {K_{II}}^{(2)} + {K_I}^{(2)} {K_{II}}^{(1)}) \quad (38)$$

If the auxiliary state (2) is assumed as the pure mode I (${K_I}^{(2)} = 1 \ and \ {K_{II}}^{(2)} = 0$) or II (${K_I}^{(2)} = 0 \ and \ {K_{II}}^{(2)} = 1$) asymptotic fields (based on Eq. (7)), the mode I SIF (${K_I}^{(1)}$) or the mode II SIF (${K_{II}}^{(1)}$) can be calculated, respectively.

Where the cracked plate has a perpendicular axis of symmetry to the crack, only the crack opening mode I is present and the crack has no sliding mode II ($K_{II} = 0$); in such cases, the mode I SIF (K_I) can be obtained from Eqs. (29)-(32).

2.6 Numerical integration

By the XFEM, the singularity occurs in the integrand of related terms, in the stiffness matrix. Those terms consist a combination of $\{1/r, 1/\sqrt{r}, 1, \sqrt{r}, r\}$ multiplied by harmonic functions, in addition to terms coming from regular shape functions. The radial parts are singular and so create difficulties for the integration. Here, the crack tip elements are divided to triangular sub-domains, in order to have continuous integrand functions on every sub-domain. In this way, singular point lies on a vertex. Béchet *at al.* (2005) found that convergence achievement by a standard Gauss integration is very slow; so clearly, a better quadrature scheme is needed. In this order, the real triangular interpolation cell is mapped to a reference quadrature cell; and hence, the singular functions are transformed into regular ones. Based on the study of Béchet *at al.* (2005), this transformation is useful to integrate singular functions, in a fast way, with significant improvements in the convergence characteristics, and within the prescribed accuracy. Béchet *at al.* (2005) indicate that considering 9 integration points would be sufficient, for the case of XFEM stiffness matrix. More details about the singular integration by the transformation scheme can be found in references (Béchet *at al.* 2005, Khoei 2014).

Fig. 3 shows the Gauss points in different types of elements existing in this study. The standard elements (type 1) use 2×2 Gauss integration. The elements cut by a crack and enriched by the Heaviside function (type 2) are divided into two quadrilateral sub-domains, and for each one 2×4 Gauss points is used. The elements with crack tip enrichments (type 3) use more sub-domains and more Gauss points due to the singular nature of stress fields in the vicinity of crack tip; hence, these elements are divided into six triangular sub-domains, and each one is mapped to a rectangular domain with 3×3 Gauss points, as depicted in Fig. 4. The elements which are not cut by a crack but they are partially enriched by crack tip enrichments (type 4) use 5×5 Gauss points. Lastly, elements cut by a crack and partially enriched by crack tip enrichments (type 5) are divided into two quadrilateral sub-domains with 3×6 Gauss points per sub-domain (Fig. 3). It should be noted that for calculating the J-integral, a 4×4 Gauss integration is performed for standard elements existing in the domain of J-integral. For all elements, 2 Gauss points through thickness are considered.

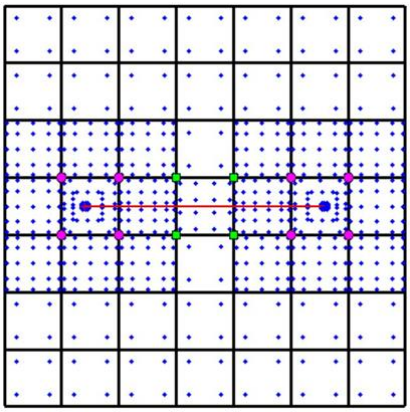

Fig. 3 Gauss points in various element types

The integration of typical function (f) on the domain of element is calculated using the following equation

$$\int_V f(\xi, \eta, \varsigma) dV = \sum_{s=1}^{N^{sub}} \sum_{k=1}^{NGp^{\varsigma_s}} \sum_{j=1}^{NGp^{\eta_s}} \sum_{i=1}^{NGp^{\xi_s}} f(\xi_i^s, \eta_j^s, \varsigma_k^s) W_i^{\xi_s} W_j^{\eta_s} W_k^{\varsigma_s} det J^{sub} det J^{elm} \quad (39)$$

where, N^{sub} is the number of sub-domains; NGp^{ς_s}, NGp^{η_s} and NGp^{ξ_s} are the number of Gauss points, and $W_i^{\varsigma_s}$, $W_j^{\eta_s}$ and $W_k^{\varsigma_s}$ are the weights of Gauss points, corresponding to the natural coordinates of each subdomain ($\xi^s, \eta^s, \varsigma^s$) (Fig. 4); J^{sub} and J^{elm} are the Jacobian matrices, corresponding to the subdomain and to the element, respectively, expressed as below

$$J^{sub} = \begin{bmatrix} \frac{\partial \xi^e}{\partial \xi^s} & \frac{\partial \eta^e}{\partial \xi^s} & \frac{\partial \varsigma^e}{\partial \xi^s} \\ \frac{\partial \xi^e}{\partial \eta^s} & \frac{\partial \eta^e}{\partial \eta^s} & \frac{\partial \varsigma^e}{\partial \eta^s} \\ \frac{\partial \xi^e}{\partial \varsigma^s} & \frac{\partial \eta^e}{\partial \varsigma^s} & \frac{\partial \varsigma^e}{\partial \varsigma^s} \end{bmatrix}, \quad (40)$$

$$J^{elm} = \begin{bmatrix} \frac{\partial x}{\partial \xi^e} & \frac{\partial y}{\partial \xi^e} & \frac{\partial z}{\partial \xi^e} \\ \frac{\partial x}{\partial \eta^e} & \frac{\partial y}{\partial \eta^e} & \frac{\partial z}{\partial \eta^e} \\ \frac{\partial x}{\partial \varsigma^e} & \frac{\partial y}{\partial \varsigma^e} & \frac{\partial z}{\partial \varsigma^e} \end{bmatrix}$$

where, $\xi^e, \eta^e, \varsigma^e$ are the natural coordinate of the element (Fig. 4).

In order to avoid the effect of shear locking, all the standard elements and sub-domains use only 1 Gauss point for integration of those parts of the standard stiffness matrix that contain transverse shear strain terms; in this way, the selective integration scheme is applied. It is noticeable that the aforementioned arrangements for the Gauss points were found by performing a large number of XFEM analyses in order to achieve more accurate results and a good mesh convergence, which are not discussed herein for brevity.

3. XFEM modeling of cracked plates

3.1 General

The geometry of a cracked plate is shown in Fig. 5. In this figure, W and L are the width and length of the plate, respectively, and a denotes the crack length. Parameters involved in numerical modeling of the cracked plate include: plate aspect ratio (L/W), crack (size) ratio (a/W), plate support conditions, and the crack location.

The considered geometrical properties of the cracked plates include: aspect ratios 0.5, 1.0, and 2.0, crack ratios 0.1, 0.2, 0.3, 0.4, 0.5, 0.6, 0.7, 0.8, and 0.9, three different boundary conditions namely SS, CS, and CC, where SS and CC denote simple and clamped supports along all four edges, respectively, and CS denotes clamped loaded edges and simply supported unloaded edges; furthermore, in some limited cases SC boundary conditions are also considered in order to better discuss the results.

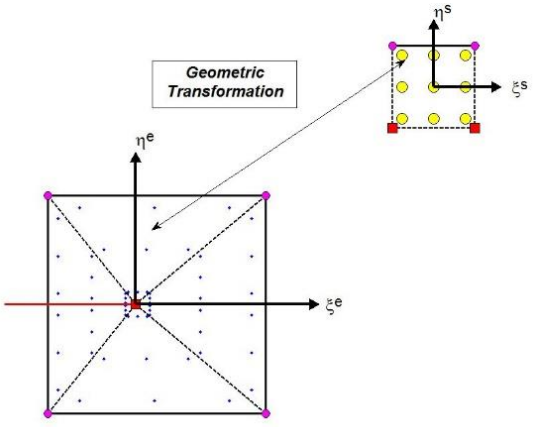

Fig. 4 Geometric transformation of a triangular sub-domain

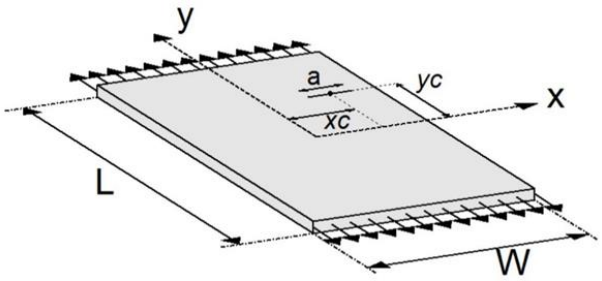

Fig. 5 Geometry of a cracked plate

The location of the crack center on the plate is characterized by two eccentricity parameters $e_x = \frac{x_c}{W/2}$ and $e_y = \frac{y_c}{L/2}$ where x_c and y_c are the distances from the center of a crack to the plate centerlines, as depicted in Fig. 5. For a central crack, the values of e_x and e_y are equal to zero and for non-central cracks, the values of $|e_x|$ and $|e_y|$ would be between (but not equal to) zero and one. Regarding the symmetry, the considered values for e_y in the present study are 0, 0.1, 0.2, 0.3, 0.4, 0.5, 0.6, 0.7, 0.8, and 0.9. The values considered for e_x would be different contingent upon the crack sizes. Consistent with all cases, the plate width (W) and thickness (t) are set to 305 cm and 2.54 cm, respectively. The material considered in this research is aluminum alloy with modulus of elasticity $E =$ 70 GPa and Poisson's ratio $\nu =$ 0.3.

Non-dimensional buckling stress coefficient (k_{cr}) and multiplier (λ_T) employed in this study to evaluate the buckling behavior of the cracked plates are defined as below

$$k_{cr} = \frac{\sigma_T}{E} \frac{12(1-\nu^2)}{\pi^2} \left(\frac{W}{t}\right)^2 \tag{41}$$

where, k_{cr} is the buckling coefficient, σ_T is the buckling stress in tension, and t is the plate thickness. Also

$$\lambda_T = \left|\frac{\sigma_T}{\sigma_E}\right| \tag{42}$$

where, λ_T is the buckling multiplier in tension and σ_E is the Euler buckling stress of the un-cracked plate under uniaxial compression which can be obtained using the well-established theoretical and/or numerical methods (Brighenti 2009).

For presenting the mode I SIF results, a dimensionless stress intensity factor (φ) is defined as below

$$\varphi = \frac{K_I}{\sigma_0 \sqrt{\frac{\pi a}{2}}} \tag{43}$$

in which φ, K_I, and σ_0 are the dimensionless SIF, mode I SIF, and applied edge stress, respectively. In addition, as defined above, a is the crack length. A XFEM code was developed using the programming software MATLAB (MATLAB 2014) for the analysis of the cracked plate models.

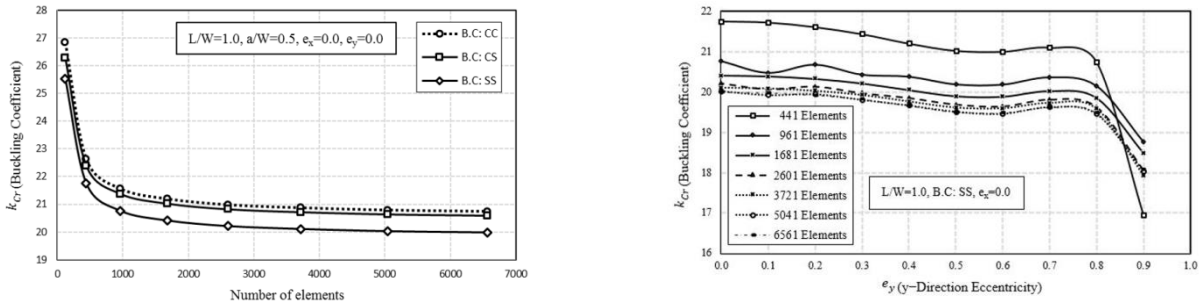

(a) (b)

Fig. 6 Mesh sensitivity analysis: (a) centrally-cracked plates with different boundary conditions and (b) non-centrally-cracked plates (with simple supports)

Table 1 Theoretical and numerical buckling coefficients for un-cracked plates

L/W	Support conditions	Buckling coefficient (k_{cr})		Percentage difference
		Theoretical (Timoshenko and Gere (1961))	Numerical (This study)	
0.5	SS	6.25	6.2011	-0.78
	CC	-	18.8966	-
	CS	-	18.1377	-
1.0	SS	4	3.9705	-0.74
	CC	10.07	10.0699	-0.001
	CS	6.74	6.7281	-0.18
2.0	SS	4	3.9781	-0.55
	CC	7.88	7.8673	-0.16
	CS	4.85	4.8332	-0.35

Table 2 Buckling multipliers for plate aspect ratio of 2.0 and different crack sizes ($L/W = 2.0$ & $e_x = e_y = 0$)

Support conditions	a/W	Buckling multiplier (λ_T)			
		(Shaw and Haung (1990))	Brighenti (2009)	This study	Difference with Brighenti (2009) (%)
Simply supported edges	0.2	40.2562	40.6830	42.7496	5.08
	0.3	-	17.8093	18.2053	2.22
	0.4	-	9.8232	10.0081	1.88
	0.5	-	6.0133	6.0977	1.40
Clamped edges	0.2	-	20.8768	21.7463	4.16
	0.3	-	9.1678	9.2912	1.35
	0.4	-	5.0392	5.0893	0.99
	0.5	-	3.1122	3.1262	0.45

3.2 Mesh convergence study

In order to check the mesh convergence towards the buckling coefficient and/or mode I SIF, several simulations were performed for cracked plate models with L/W =1.0, a/W =0.5, and different uniform mesh sizes. The effect of integration radius on the mode I SIF was investigated as well. The sensitivity of k_{cr} to the number of elements is illustrated in Fig. 6 for centrally- and non-centrally-cracked plates; however, the details of the SIF sensitivity analyses are not given in here. In order to ensure accuracy in the results for k_{cr} and φ, a mesh containing 5041 (71×71) elements was chosen. For calculating the J-integral, the selected radius of integration was equal to the three times the diameter of the element.

Table 3 Dimensionless SIF for plate aspect ratio of 2.0 and different crack sizes ($e_x = e_y = 0$)

L/W	a/W	Dimensionless SIF (φ)			Difference with Brighenti (2009) (%)
		Isida (1971)	Brighenti (2009)	This study	
2.0	0.2	1.0233	1.0386	1.0041	-3.32
	0.3	1.0581	1.0476	1.0525	0.47
	0.4	1.1116	1.1145	1.1044	-0.91
	0.5	1.1860	1.1921	1.1813	-0.91

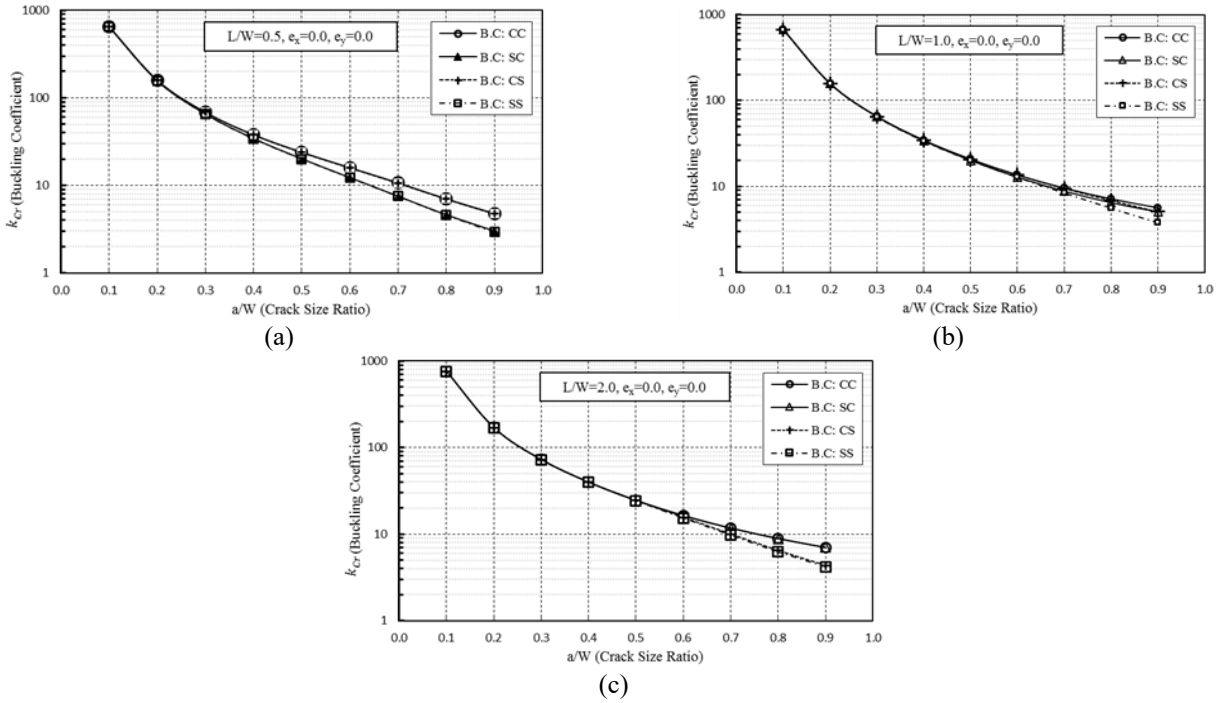

(a) (b) (c)

Fig. 7 Buckling coefficient vs. crack size ratio for centrally-cracked plates with different boundary conditions and aspect ratios of (a) 0.5; (b) 1.0 and (c) 2.0

3.3 Model verification

To verify the validity of the numerical simulation, the numerical predictions of this study are compared with some reliable references available in the literature. The theoretical and numerical buckling coefficients for un-cracked plates are compared in Table 1. Also, the buckling multipliers for plates with an aspect ratio of 2.0 ($L/W = 2.0$), different crack sizes, and $e_x = e_y = 0$ are compared in Table 2. Additionally, Table 3 summarizes the dimensionless SIF results for plates with an aspect ratio of 2.0, different crack sizes, and $e_x = e_y = 0$. The tabulated results are indicative of accuracy of the numerical predictions of the present study.

4. Results and discussion

The obtained numerical results give useful information about the buckling behavior and SIF of cracked plates under tension. In this section, these results are presented in three subsections including the centrally-cracked plates, cracked plates with eccentricity in y-direction (e_y), and cracked plates with eccentricity in x and y-directions (e_x and e_y). In all subsections, the effects of different parameters such as the plate aspect ratio, crack size ratio, boundary conditions, and crack location on the buckling coefficient, mode shapes, and dimensionless SIF are investigated.

4.1 Centrally-cracked plates

The effect of crack size on the buckling coefficient of centrally-cracked plates under tension is illustrated in Fig. 7. Unlike the results reported for many cases of compressed cracked plates (Brighenti 2009, Khedmati *et al*. 2009), in plates under tension, increasing of the crack size always results in the reduction of the buckling coefficient. It is also observed that boundary conditions have a little effect (less than 2%) on the buckling coefficients of plates with a small crack (crack size ratio of 0.1 and 0.2); however, with increasing of the crack size, the buckling coefficient is more affected by the boundary conditions; such that, the coefficients for SS and CC conditions are obviously different in the cases of large cracks (a/W =0.7, 0.8, and 0.9).

As seen in Fig. 7(a) for the aspect ratio of 0.5, the curves

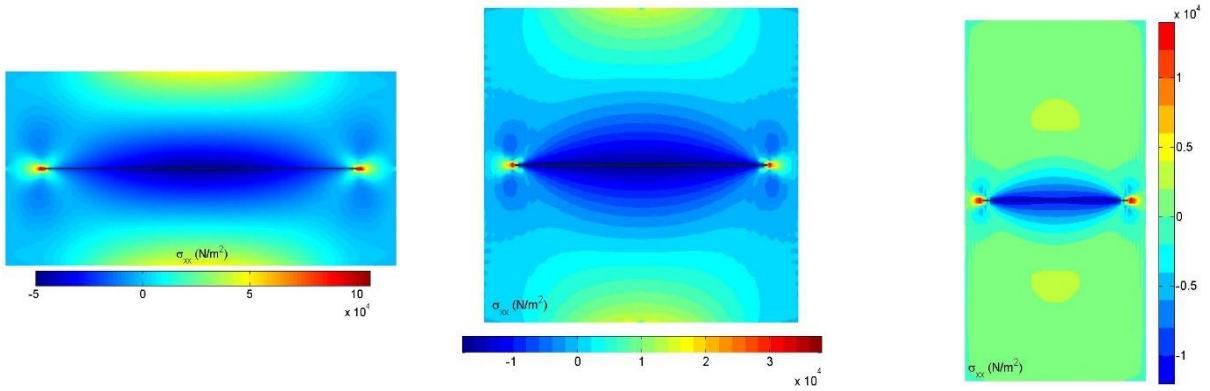

(a) (b) (c)

Fig. 8 Compressive areas around the crack edges (dark and light blue) for plates with aspect ratios of (a) 0.5, (b) 1.0 and (c) 2.0

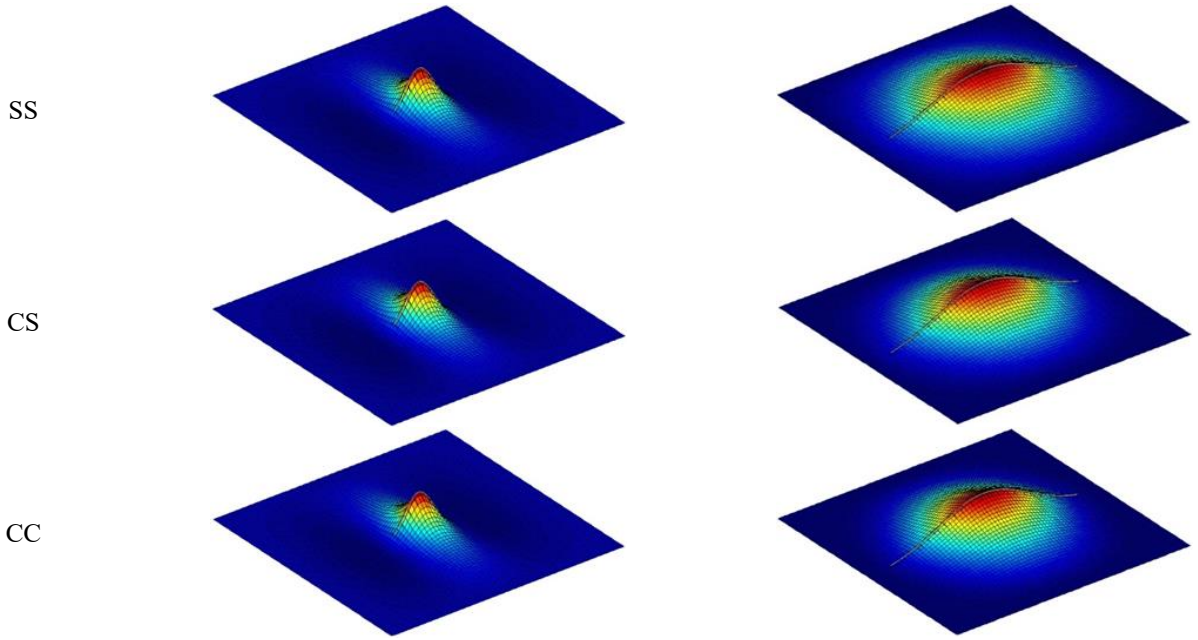

(a) a/W =0.2 (b) a/W =0.8

Fig. 9 First buckling mode shapes for plates with different support conditions and a/W ratios (L/W =1.0)

corresponding to CS and CC support conditions and also the curves corresponding to SC and SS support conditions are very close, while this observation is vice versa for the aspect ratio of 2.0 (Fig. 7(c)) in which the curves of SC and CC support conditions and also CS and SS support conditions are very close. This is attributed to the fact that tensioned cracked plates undergo localized buckling and those plate edges that are far from the compressive areas of the crack faces (shown in Figs. 8(a)-8(c)) play a negligible role in the buckling; therefore, the unloading and loading edges in plates with aspect ratios of 0.5 and 2.0, respectively, have negligible effects on the buckling coefficient. For instance, in the case of a/W =0.8, clamping the loaded edges (CS) increases the buckling coefficient by 52% and 3.5% for respective aspect ratios of 0.5 and 2.0, while clamping the unloaded edges (SC) increases the coefficient by 0.5% and 43% for the aforementioned respective aspect ratios.

As shown in Fig. 8(b) for the case of L/W =1.0, the distances of loading and unloading edges to the crack compressive area are roughly the same; hence, for the above-mentioned reason, the curves corresponding to SC and CS conditions are close to each other (Fig. 7(b)) in this case. As an example, in the case of a/W =0.8, clamping separately the loading edges (CS) and/or unloading edges (SC) increases the buckling coefficients by 22% and 16%, respectively.

In Fig. 9, the first buckling mode shapes for tensioned cracked plates are displayed for the cases corresponding to SS, CS, and CC support conditions. As seen in Fig. 9(a) and consistent with the findings reported in Brighenti 2005, Brighenti 2005, Brighenti 2009, buckling mode shapes of

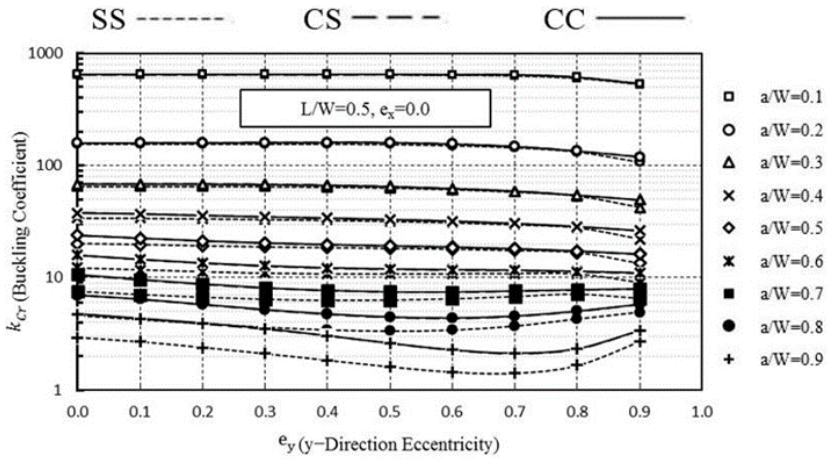

(a)

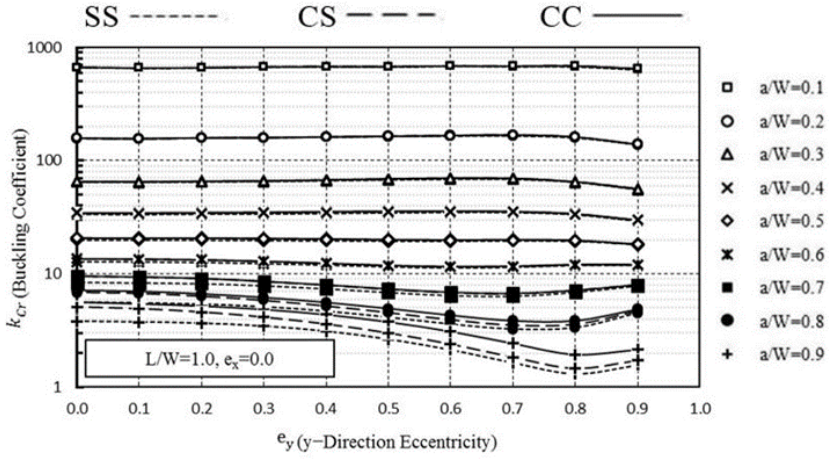

(b)

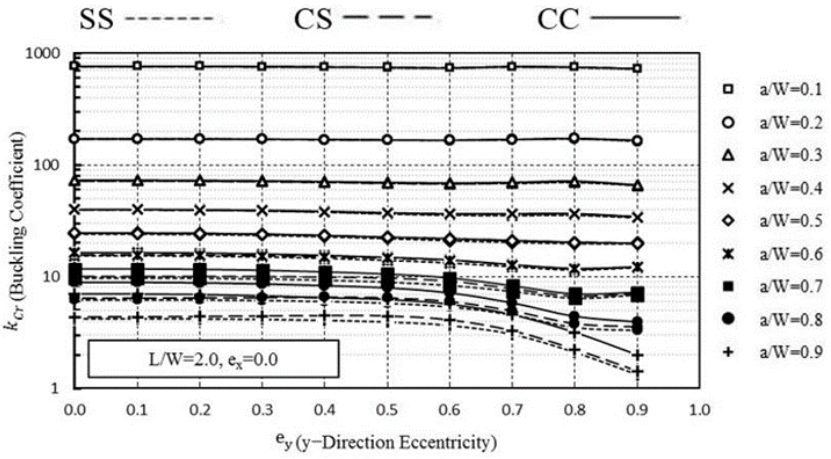

(c)

Fig. 10 Buckling coefficient vs. e_y for cracked plates with (a) $L/W = 0.5$, (b) $L/W = 1.0$ and (c) $L/W = 2.0$

the tensioned plates with small- or medium-length cracks, i.e., $a/W \leq 0.6$, are localized around the crack area and seem to be slightly or even not affected by the different boundary conditions. Based on the results of the present study for the case of large cracks, it is found that by increasing of the crack size, buckling mode shapes tend to change to a semi-global instability with large and diffuse out-of-plane displacements, as illustrated in Fig. 9(b).

4.2 Cracked plates with eccentricity in y-direction

Fig. 10 shows the plots of the buckling coefficient (k_{cr})

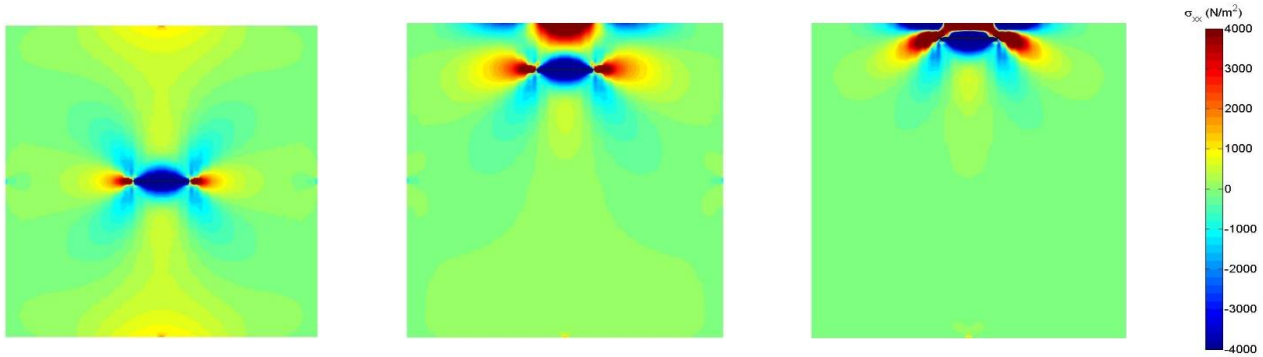

(a) $e_y = 0$ (b) $e_y = 0.7$ (c) $e_y = 0.9$

Fig. 11 Stress field (σ_{xx}) in a cracked plate with aspect ratio of 1, $a/W = 0.2$, and various e_y eccentricities

versus eccentricity in y-direction ($e_y = \frac{y_c}{L/2}$) for different plate aspect ratios and boundary conditions. It is observed that increasing of the crack size for a given eccentricity results in decreasing of the buckling coefficient. From Fig. 10, in case of the small cracks, the effect of the crack eccentricity on the buckling coefficient is not notable, except for very high eccentricities where the coefficient decreases slightly. This can explained by considering the results of Fig. 11 where the σ_{xx} stress field obtained from pre-buckling in-plane analysis of the cracked plate under unit tension load per edge length is shown. As seen, greater compressive stresses are developed in the case of e_y =0.9 (Fig. 11(c)) rather than the cases of $e_y = 0$ (Fig. 11(a)) and $e_y = 0.7$ (Fig. 11(b)); in fact, development of such considerable compressive stresses in cases of very high eccentricities is effective in lowering the buckling coefficient.

For the case of large cracks, variation of the buckling coefficient is different depending on the plate aspect ratio and the crack eccentricity (Fig. 10). This behavior can be explained by referring to the σ_{xx} stress field shown in Fig. 12 for different plate aspect ratios and eccentricities. The depicted results of Figs. 10 and 12 indicate that increasing of the eccentricity results in the development of greater compressive stresses which, in turn, lowers the buckling coefficient generally. Although, according to Fig. 10 for large cracks in L/W <=1.0, a minima in the curves can be observed; this observation is explainable by focusing on Fig. 12. As seen, the minima point is just corresponding to the condition in which there is the maximum compressive area around the crack. Furthermore, comparison of the results shown in Figs. 11 and 12 reveals that the stresses developed around the large crack tips are significantly greater than those of the small cracks. This finding is expected, since the mode I SIF (K_I) is directly related with the square root of crack length (Broek 1974). In addition, as seen in Fig. 12, large cracks located in the vicinity of the loading edge (with high eccentricity) experience larger tensile stresses at the areas near the crack tips, while relatively lower stresses are developed in cracks with no (central) or low eccentricities. So, it can be concluded that the SIF is a crack eccentricity-related parameter and the stress field can be determined by employing the concept of SIF (Khoei 2014). Past research on SIF has been largely limited to central cracked plates (Kaman and Cetisli 2012); however, this research studies the SIF in non-central cracked plates. It should be noted that, as mentioned earlier, in cracked plates with eccentricity in only y-direction, there is no sliding mode II, because of the symmetry.

In order to further investigate the effect of crack eccentricity on K_I, the dimensionless SIF (φ) is plotted against the y-direction eccentricity (e_y) for plates with different aspect ratios as seen in Fig. 13. It is evident that SIF increases by increasing of the crack eccentricity. The rate of this increase is higher in cases of larger cracks. This finding is consistent with the results of Fig. 12 where greater stresses are developed around the tips of the cracks with higher eccentricity. In case of small cracks, SIF is not remarkably affected by the variation of eccentricity (Fig. 13). Fig. 13, also, shows that plate aspect ratio can be effective on the value of SIF, particularly in plates with larger crack sizes. As seen in Figs. 13(a)-13(c), the value of φ increases by decreasing of the L/W ratio.

To evaluate the effect of support conditions, the relative difference in k_{cr} of the clamped plates (CC) and that of the corresponding simply supported ones (SS) is illustrated in Fig. 14 for different crack length ratios. As shown in Figs. 14(b) and 14(c), in the cases of plates with aspect ratios 1.0 and 2.0 having small and medium size cracks ($a/W \leq 0.6$), the effect of support conditions on k_{cr} is up to 8%. Nevertheless, for plates with large cracks, the effect of the support conditions is significant; for instance, in the plate with $L/W = 2.0$ and $a/W = 0.9$, this effect is up to 70% for the central crack. Also, it is found that the effect of the support conditions is more considerable for plates with central cracks rather than those with eccentric ones.

Table 4 provides the critical mode shapes of the simply-supported and clamped cracked plates with $a/W = 0.8$ and different aspect ratios. From the table, the boundary conditions may alter the buckling mode shape; for instance, the buckling mode shapes of the plates with $L/W = 0.5$ and $e_y = 0$ and 0.9 are affected by the SS and CC support conditions.

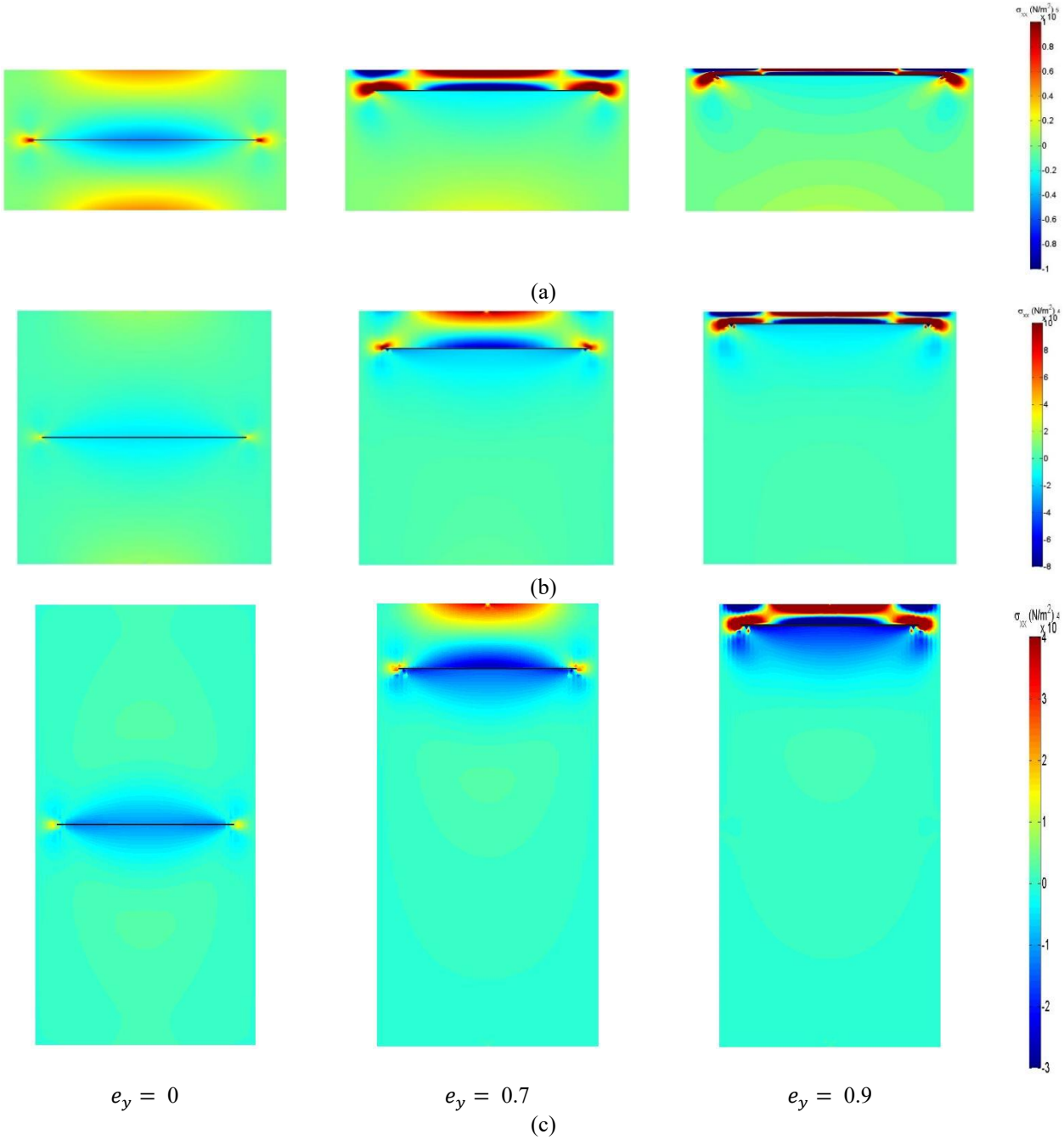

Fig. 12 Stress field (σ_{xx}) in a cracked plate with $a/W = 0.8$ and aspect ratios of (a) $L/W = 0.5$, (b) $L/W = 1.0$ and (c) $L/W = 2.0$

In order to be able to evaluate k_{cr} and φ in different common practical cases characterized by the geometrical parameters ranging in the considered intervals, the logarithm of the results have been interpolated by using a weighted least square fitting with 8th-order polynomial expression. The maximum errors in this way for k_{cr} and φ in the considered ranges are about 1.8% and 4.6%, respectively.

To answer the question: "will a plate under tension collapse due to buckling or fracture?", the following equation can be used based on Brighenti (2009) for calculating the value of buckling-fracture collapse function (F_{col})

$$F_{col} = \frac{\beta^2}{\pi.\frac{a}{2}} - {\lambda_T}^2.\varphi^2 \tag{44}$$

where, λ_T is the buckling multiplier in tension (Eq. (42)), φ is the dimensionless stress intensity (SIF) factor (Eq. (43)), a is the crack length, and β is the fracture toughness parameter defined as Brighenti (2009)

$$\beta = \frac{K_{IC}}{\sigma_E} \tag{45}$$

Table 4 Critical mode shapes of plates with a/W =0.8 and various boundary conditions

L/W	B.C.	e_y = 0	e_y = 0.7	e_y = 0.9
0.5	SS	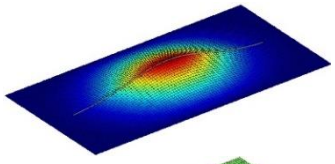	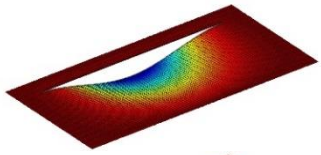	
	CC	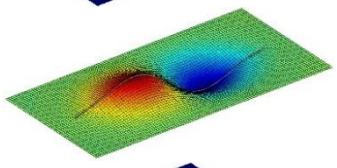	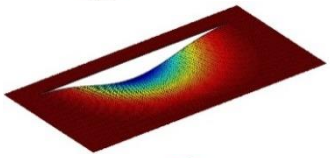	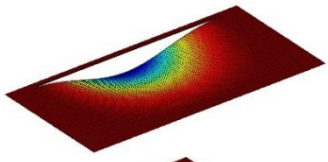
1.0	SS	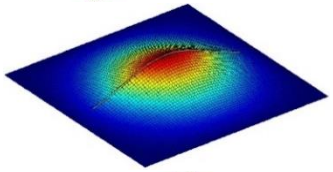	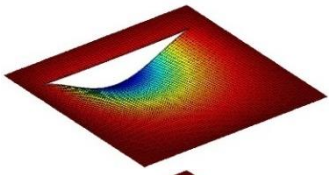	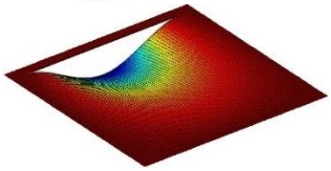
	CC	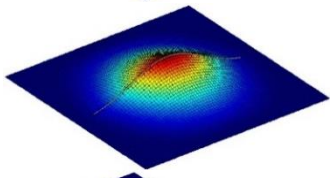	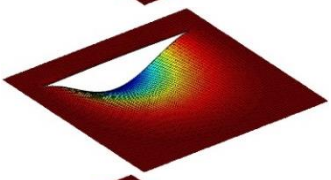	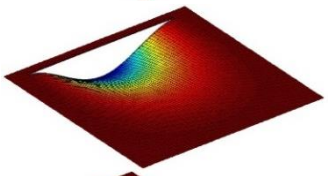
2.0	SS	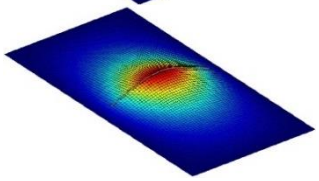	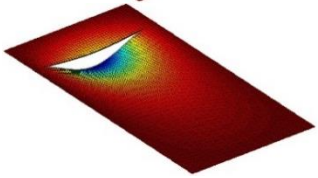	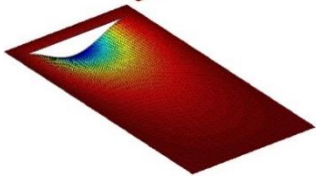
	CC	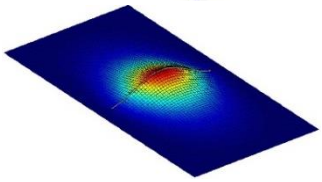	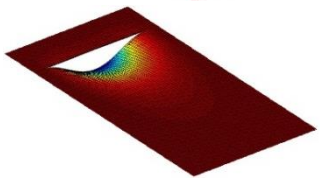	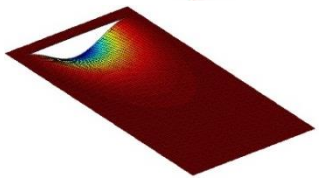

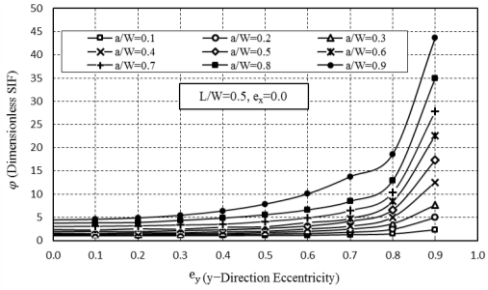

(a)

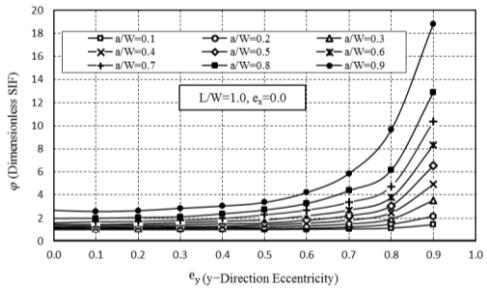

(b)

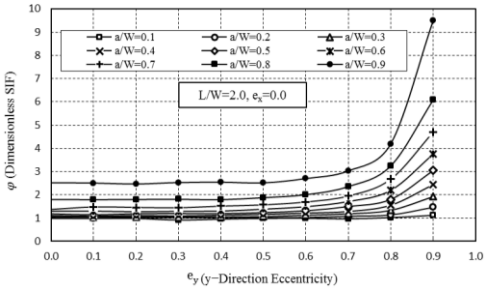

(c)

Fig. 13 Dimensionless SIF (φ) vs. eccentricity (e_y) for cracked plates with (a) L/W = 0.5, (b) L/W = 1.0 and (c) L/W = 2.0

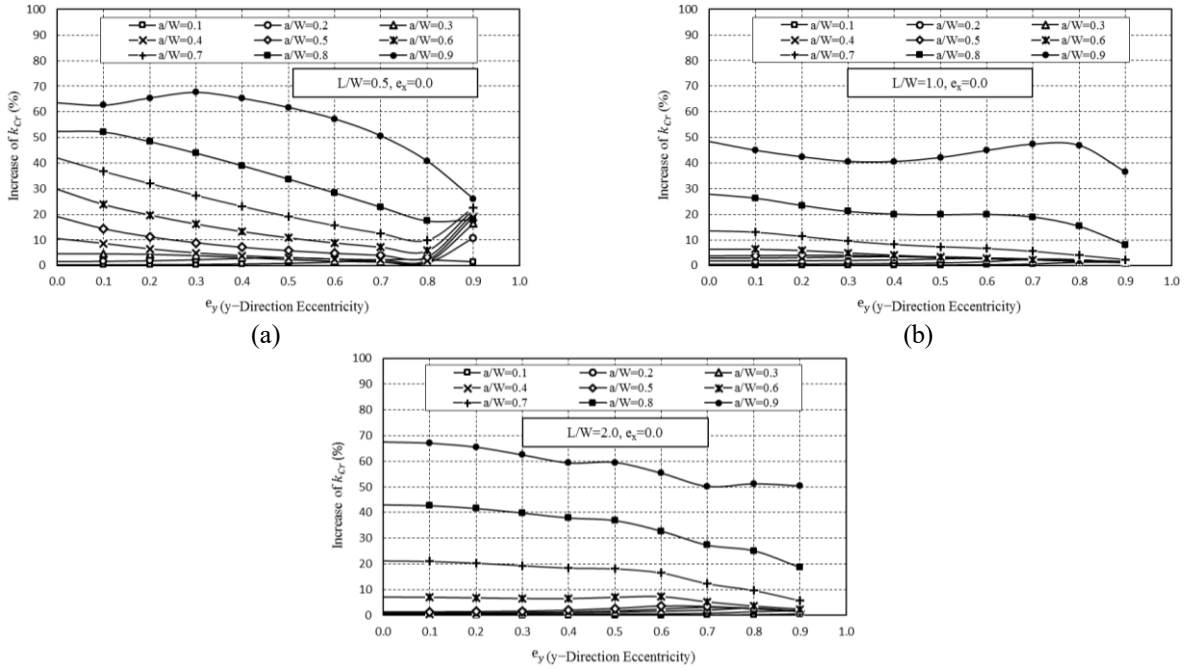

(a) (b) (c)

Fig. 14 Increase of k_{cr} due to clamping of the edges of simply supported cracked plates with (a) $L/W = 0.5$, (b) $L/W = 1.0$ and (c) $L/W = 2.0$

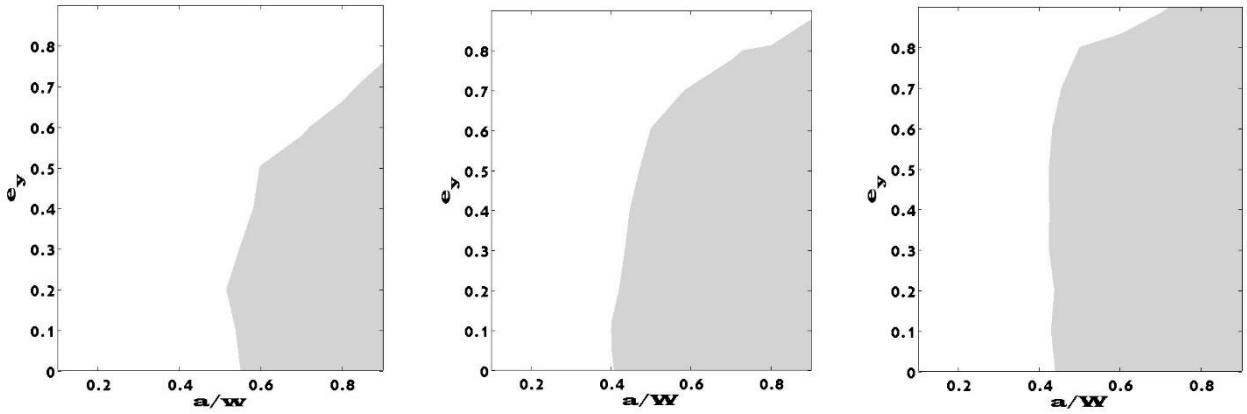

(a) $L/W = 0.5$ (b) $L/W = 1.0$ (c) $L/W = 2.0$

Fig. 15 Plots of e_y (vertical) vs. a/W (horizontal) for simply supported cracked plates with different aspect ratios *(shaded area = region of buckling collapse; white area = region of fracture collapse)*

in which, K_{IC} is the critical value of the mode I stress intensity factor corresponding to the material of the plate and σ_E is the Euler buckling stress for uncracked plate depending on the aspect ratio (L/W), width-to-thickness ratio (W/t), and material properties E and ν of the plate. In Eq. (44), if the value of the buckling-fracture collapse function is found to be higher than zero ($F_{col} > 0$) then the buckling collapse will occur, and if its value is found to be lower than zero ($F_{col} < 0$) then the fracture collapse will take place (Brighenti 2009).

Through the assessment of the parameter β from Eq. (45), a region for the present study's domain ($\Omega = (0.1 \leq \left(\frac{a}{W}\right) \leq 0.9 \; ; \; 0 \leq e_y \leq 0.9 \; ; e_x = 0.0)$ corresponding to the buckling collapse can be specified by using Eq. (45). For aluminum alloy, $K_{IC} = 40.7 \; MPa\sqrt{m}$ (Brighenti 2009) and σ_E can be calculated using Table 1.

As mentioned before, σ_E depends on the width-to-thickness ratio (W/t). Assuming W/t =120, the value of the buckling-fracture collapse function (F_{col}) would be negative and this is indicative of the occurrence of the fracture collapse in the previously-defined domain. Since

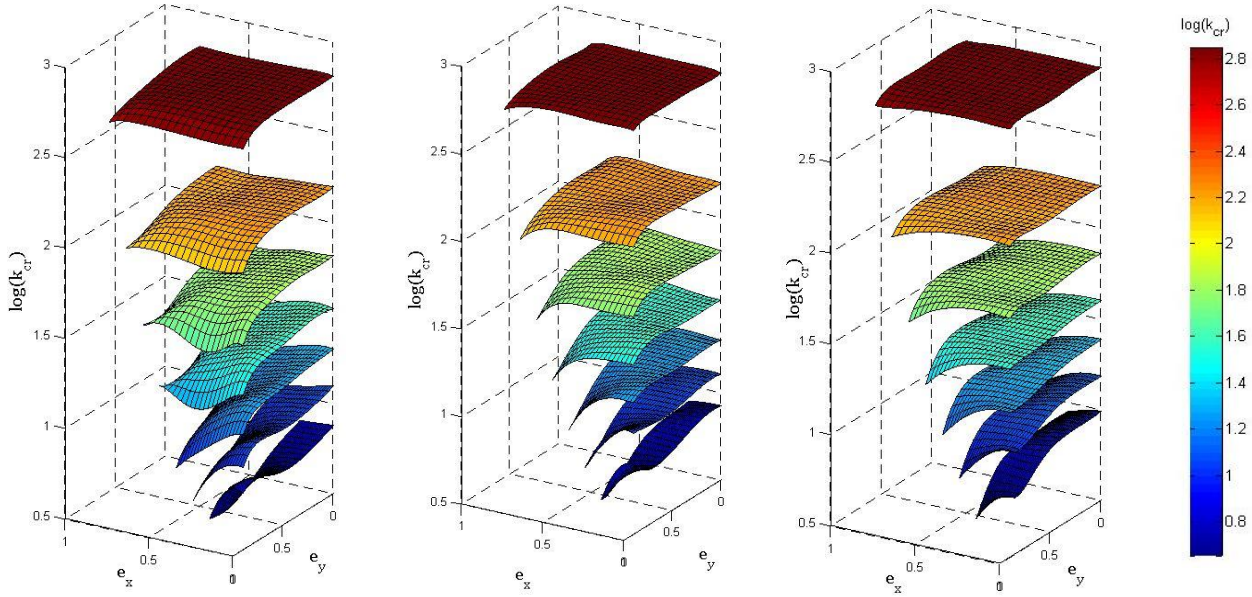

(a) $L/W = 0.5$ (b) $L/W = 1.0$ (c) $L/W = 2.0$

Fig. 16 Fitted surfaces of k_{cr} for simply supported cracked plates with (a) $L/W = 0.5$, (b) $L/W = 1.0$ and (c) $L/W = 2.0$

(Surfaces for $\frac{a}{W} = 0.1$ to $\frac{a}{W} = 0.7$ are top to bottom respectively.)

the parameters λ_T and φ are independent of the material properties K_{IC}, E, and ν as well as the W/t ratio, the function F_{col} can be calculated for different values of W/t using the previous results. In Fig. 15, the regions corresponding to the buckling collapse are illustrated for simply supported aluminum alloy plates with W/t =400 and different aspect ratios.

As shown in Fig. 15, plates with small cracks are always subjected to fracture collapse under ultimate tensile loading, without experiencing the buckling. In addition, it is seen that the possibility of this failure mode decreases for plates with larger cracks and/or smaller eccentricities (e_y). Moreover, it is found that by increasing of the aspect ratio, the shaded area corresponding to the buckling collapse increases. The findings of the current research endeavor also indicate that the plate support conditions do not have a notable effect on the areas of the buckling-fracture collapse regions. The results related to the other boundary conditions have not presented here for brevity.

4.3 Cracked plates with eccentricities in x- and y-directions

In order to investigate the effect of crack location on the buckling and fracture failure modes, 1450 plates with bi-eccentric cracks were modeled. For presenting the results, an interpolation function is considered as a 6th-order polynomial which was obtained by using a weighted least square fitting. The maximum errors in this way for k_{cr} and φ are about 8.67% and 12.16%, respectively. Figs. 16 and 17 show the graphical results of the fitted surfaces for simply supported cracked plates with 0.1-0.7 crack sizes and different aspect ratios.

As seen in Fig. 16, the fitted surfaces do not intersect. This indicates that for a plate with a crack located at a specified location, increasing of the crack length generally results in decreasing of the buckling load. Also, Fig. 16 shows that buckling coefficient is more sensitive to the crack length rather than the location of the crack. Moreover, it is found that near-the-corner located cracks are more effective in lowering the buckling capacity than those placed at other locations; therefore, considering plates with central cracks for representing the cracked plates is not a conservative approach to study the stability performance of such plates.

Fig. 17 shows that the mode I SIF of the crack tips located near the plate edges is significantly higher than that of the crack tips far from the edges. As seen, the eccentricity in y-direction is more effective on mode I SIF than the eccentricity in x-direction. The results of the present study, also, indicate that from the two tips of a crack, the one closer to the plate edge has relatively higher mode I SIF. In addition, Fig. 17(a)-17(c) shows that for a given crack size and an eccentricity, decreasing of the aspect ratio results in increasing of the mode I SIF.

While Figs. 16 and 17 depict the results for small- and medium-size cracks, the results corresponding to large-size cracks are illustrated in Figs. 18 and 19. From Fig. 18, it is evident that by increasing of e_y, consistent with most of the cases, the buckling coefficient decreases initially and then at higher eccentricities increases slightly. Fig. 19 shows that in case of the large cracks, as well, mode I SIF increases when the crack tip gets closer to the loaded edge; however, this increase is rather significant relative to those of the small-and medium-size cracks.

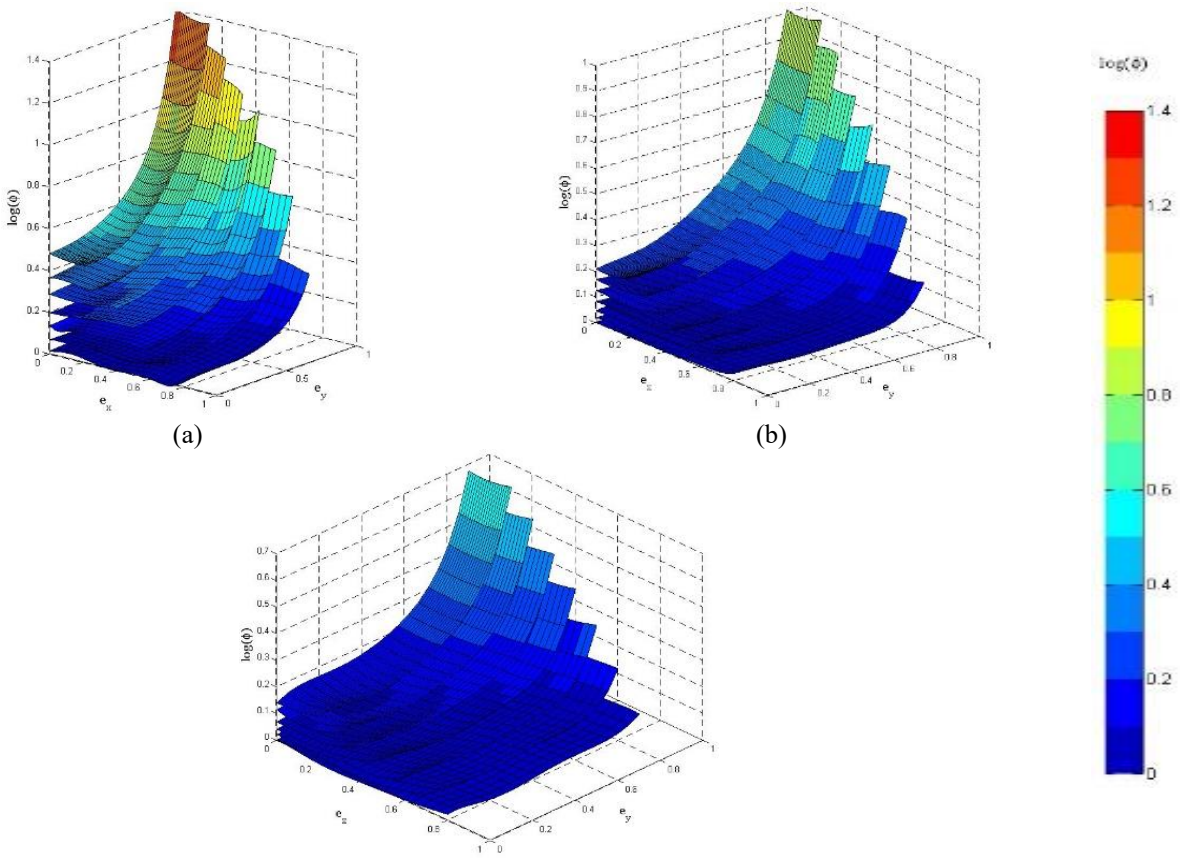

Fig. 17 Fitted surfaces of φ for cracked plates; (a) $L/W = 0.5$, (b) $L/W = 1.0$ and (c) $L/W = 2.0$
(The value of φ is related to the crack tip that is closer to the edge of plate.)
(Surfaces for $\frac{a}{W} = 0.1$ to $\frac{a}{W} = 0.7$ are top to bottom respectively.)

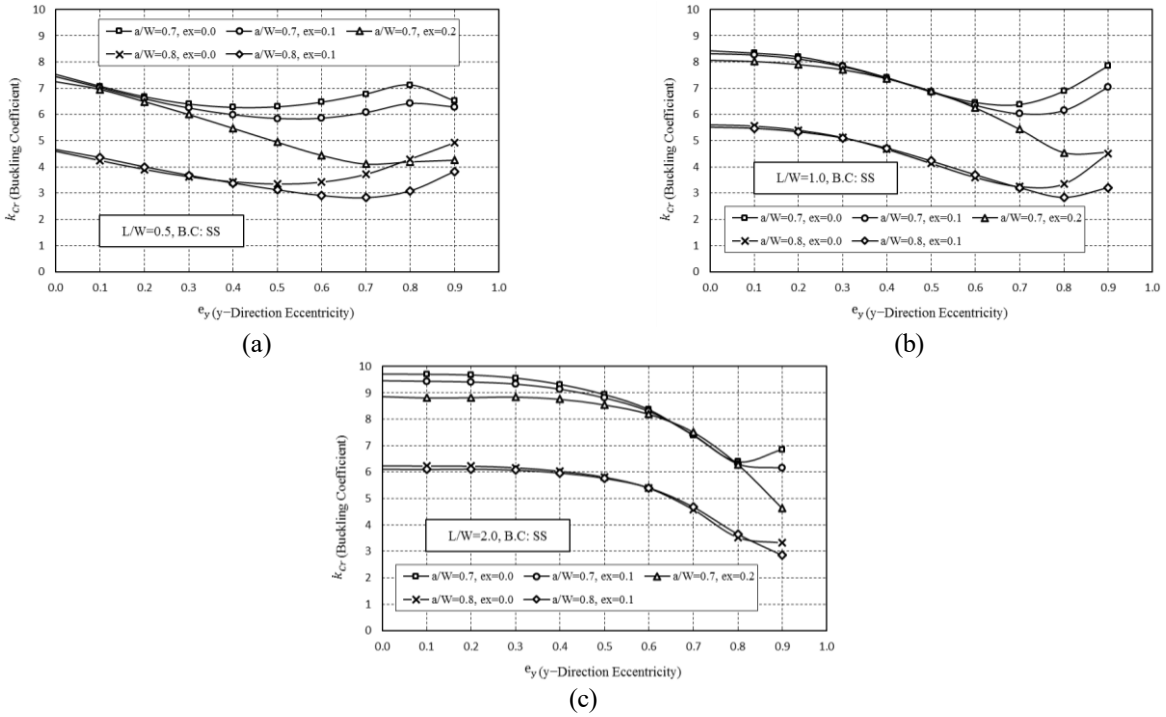

Fig. 18 Buckling coefficient vs. e_y for simply supported cracked plates With (a) $L/W = 0.5$, (b) $L/W = 1.0$ and (c) $L/W = 2.0$

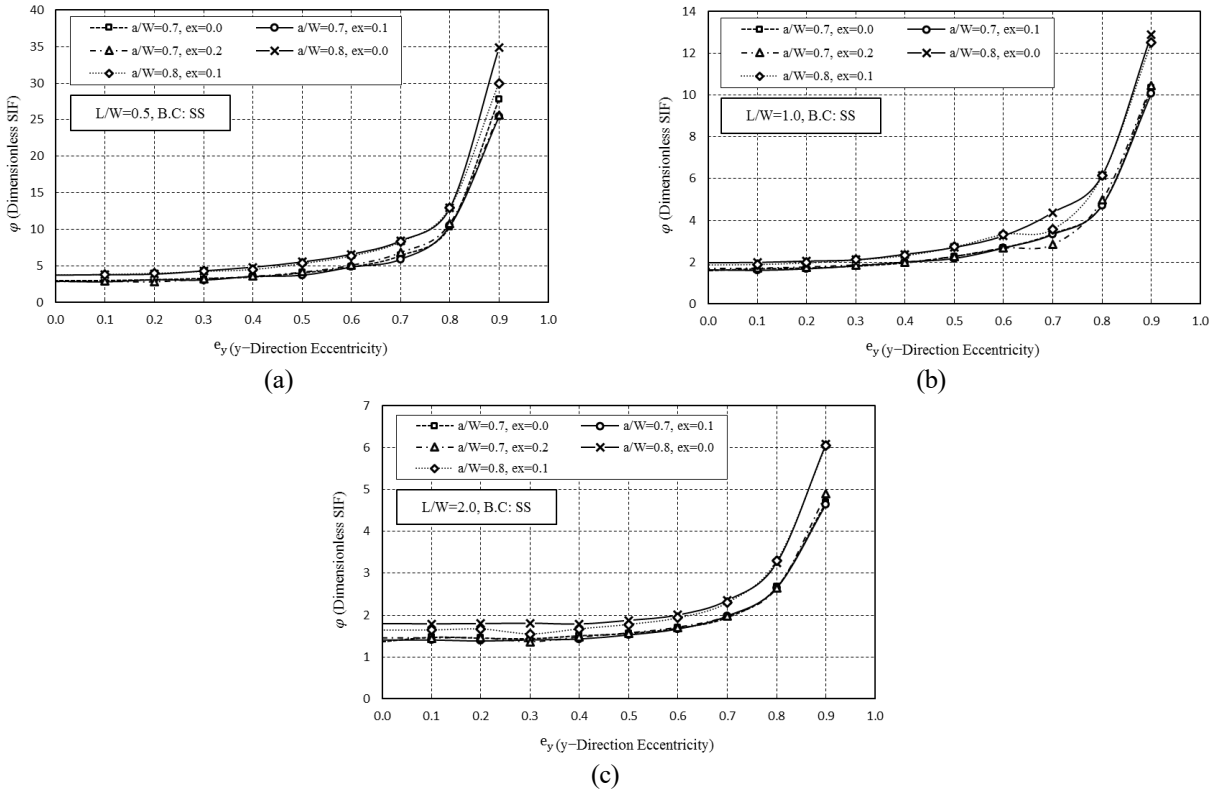

Fig. 19 Dimensionless SIF (φ) vs. eccentricity (e_y) for cracked plates with (a) $L/W = 0.5$, (b) $L/W = 1.0$ and (c) $L/W = 2.0$

(The value of φ is related to the crack tip that is closer to the edge of plate.)

Regarding Figs. 16 and 18, there is not a general condition for the un-safest crack location wherein the buckling failure occurs; while, that depends on the crack length and the plate aspect ratio. On the other hand, as seen in Figs. 17 and 19 for the fracture failure, it can be said that in most cases, the un-safest condition is when the crack is located near the plate edges.

In cases that the crack is placed non-symmetrically inside the plate, the existence of the sliding mode II, in addition to opening mode I is expected. However, the results of the present study for tensioned cracked plates showed that the sliding mode II has no effective contribution in mixed mode SIF and consequently in the value of the energy release rate (Eq. (32)). For a typical example in which sliding mode II has the most contribution in the energy release rate, among the cases studied here, the ratio of mode I to mode II SIFs (K_I/K_{II}) is 8, related to the cracked plate with $L/W = 0.5$, $a/W = 0.3$, $e_x = 0.5$, and $e_y = 0.6$; since, in Eq. (32) for calculating energy release rate, the SIF is of order of 2, then the contribution of K_{II} is 1/64 of the contribution of K_I and it can be ignored. Fig. 20 shows the deformation of the mentioned typical case. As seen, the opening mode I of crack is significantly dominant. Therefore, the effect of crack length and location on mode II SIF has not presented in this paper.

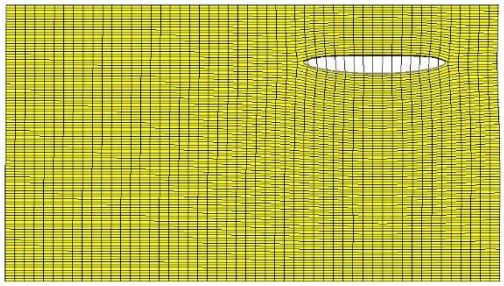

Fig. 20 Deformed cracked plate under tension

5. Conclusions

In this paper, the effects of various parameters on the buckling stability performance of the cracked plates under tensile loading were investigated. The considered parameters included the crack length, crack location, and plate aspect ratio as well as support conditions. To fulfill the objectives of the present study, a sophisticated code was developed using MATLAB in the framework of XFEM. The cracks were categorized as small, medium, and large. Simple and clamped support conditions as well as plate aspect ratios of 0.5, 1.0, and 2.0 were considered. From the results and findings of this study, the following conclusions are drawn:

- The buckling coefficient is more sensitive to the crack length rather than the location of the crack. In cracked plates under tension, unlike those subjected to compression, increasing of the crack size results in the reduction of the buckling coefficient. This result is consistent for both centrally- and non-centrally cracked plates.
- Buckling of the plates under tension with small-and medium-size cracks ($a/W \leq 0.6$) is localized around the crack area and seems to be less or even not influenced by the different boundary conditions. According to the results of the present study for the case of large cracks, by increasing of the crack size, buckling mode shape tends to change to a semi-global instability with large and diffuse out-of-plane displacements.
- The effect of the crack eccentricity on the buckling coefficient depends on the size of the crack and in some cases on the plate aspect ratio. For small cracks, this effect is not notable, except for the cases with high eccentricity in which the buckling coefficient decreases. For large cracks, there is a discrepancy in the effect of eccentricity which would be different depending on the plate aspect ratio. The performance of plates with medium-size cracks lies in between those of the plates with small and large cracks.
- On the basis of the findings of this study, cracks located near the corner of a plate are more effective in lowering the buckling capacity than those placed at other locations. Accordingly, consideration of the crack location is quite important in the buckling stability assessment of the plates.
- Plate support conditions have little effect (less than 8%) on the buckling coefficients of the plates with small-and medium-size cracks ($a/W \leq 0.6$); however, by increasing of the crack size, the effectiveness of the boundary conditions increases, such that for large cracks, this effect might be significant (up to 70%). This study shows that the effect of boundary conditions is generally more considerable in plates with central cracks rather than those with eccentric cracks.
- The SIF evidently increases due to increasing of the crack eccentricity for larger crack sizes. In small cracks, SIF is almost not affected by the eccentricity. Plate aspect ratio may influence the SIF particularly in case of the larger cracks where the SIF for $L/W = 0.5$ was found to be higher than those for the aspect ratios of 1.0 and 2.0.

Finally, plates with small cracks under tensile loading are always subjected to fracture rather than the buckling failure mode. By increasing of the crack size, particularly for the lower crack eccentricities, the possibility of this type of collapse (fracture) decreases. For plates with larger aspect ratios, the occurrence of buckling is more probable relative to the fracture collapse, where the out-of-plane boundary conditions do not have a notable effect on the failure mode.

References

Amiri Rad, A. and Panahandeh-Shahraki, D. (2014), "Buckling of cracked functionally graded plates under tension", *Thin-Wall. Struct.*, **84**, 26-33. https://doi.org/10.1016/j.tws.2014.05.005.

Bathe, K.J. (1996), Finite Element Procedures, New Jersey: Prentice Hall.

Bayesteh, H. and Mohammadi, S. (2011), "XFEM fracture analysis of shells: The effect of crack tip enrichments", *Comput. Mater. Sci.*, **50**(10), 2793-2813. https://doi.org/10.1016/j.commatsci.2011.04.034.

Béchet, E., Minnebo, H., Moës, N. and Burgardt, B. (2005), "Improved implementation and robustness study of the X-FEM for stress analysis around cracks", *Int. J. Numer. Method. Eng.*, **64**, 1033-1056. https://doi.org/10.1002/nme.1386.

Brighenti, R. (2005), "Numerical buckling analysis of compressed and tensioned cracked thin plates", *Eng. Struct.*, **27**(2), 265-276. https://doi.org/10.1016/j.engstruct.2004.10.006.

Brighenti, R. (2009), "Buckling sensitivity analysis of cracked thin plates under membrane tension or compression loading", *Nuclear Eng. Design*, **239**(6), 965-980. https://doi.org/10.1016/j.nucengdes.2009.01.008.

Brighenti, R. and Carpintery, A. (2011), "Buckling and fracture behavior of cracked thin plates under shear loading", *Mater. Design*, **32**(3), 1347-1355. https://doi.org/10.1016/j.matdes.2010.09.018.

Broek, D. (1974), Elementary Engineering Fracture Mechanics, Noordhoff International Publishing, Leyden.

Cheng, B. and Chun, L. (2012), "Buckling behavior of strengthened perforated plates under shear loading", *Steel Compos. Struct.*, **13**(4), 367-382. https://doi.org/10.12989/scs.2012.13.4.367.

Cook, R.D. (2007), Concepts and Applications of Finite Element Analysis, John Wiley & Sons.

Dolbow, J., Moës, N. and Belytschko, T. (2000), "Modeling fracture in Mindlin-Reissner plates with the extended finite element method", *Int. J. Solids Struct.*, **37**(48-50), 7161-7183. https://doi.org/10.1016/S0020-7683(00)00194-3.

Isida, M. (1971), "Effect of width and length on stress intensity factors of internally cracked plates under various boundary conditions", *Int. J. Fracture Mech.*, **7**(3), 301-316. https://doi.org/10.1007/BF00184306.

Kaman, M.O. and Cetisli, F. (2012), "Numerical analysis of center cracked orthotropic FGM plate: Crack and material axes differ by *θ*º", *Steel Compos. Struct.*, **13**(2), 187-206. https://doi.org/10.12989/scs.2012.13.2.187.

Khedmati, M.R. and Edalat, P. and Javidruzi, M. (2009), "Sensitivity analysis of the elastic buckling of cracked plate elements under axial compression", *Thin-Wall. Struct.*, **47(**5), 522-536. https://doi.org/10.1016/j.tws.2008.10.018.

Khoei, A.R. (2014), Extended Finite Element Method: Theory and Applications, Chichester: John Wiley & Sons.

Lei, Z. and Zhang, Y. (2018), "Characterizing buckling behavior of matrix-cracked hybrid plates containing CNTR-FG layers", *Steel Compos. Struct.*, **28**(4), 495-508. https://doi.org/10.12989/scs.2018.28.4.405.

Liu, P., Bui, T.Q., Zhu, D., Yu, T.T., Wang, J.W., Yin, S.H. and Hirose, S. (2015), "Buckling failure analysis of cracked functionally graded plates by a stabilized discrete shear gap extended 3-node triangular plate element", *Compos. Part B*, **77**, 179-193. https://doi.org/10.1016/j.compositesb.2015.03.036Get rights and content.

MATLAB, R. (2014), The Mathworks, Inc., Natick.

Mohammadi, S. (2008), Extended Finite Element Method for Fracture Analysis of Structures, Malden, MA: Blackwell Publishing.

Nasirmanesh, A. and Mohammadi, S. (2015), "XFEM buckling analysis of cracked composite plates", *Compos. Struct.*, **131**, 333-343. https://doi.org/10.1016/j.compstruct.2015.05.013.

Pan, Z., Cheng, Y. and Liu, J. (2013), "A semi-analytical analysis of elastic buckling of cracked thin plates under axial compression using actual non-uniform stress distribution", *Thin-Wall. Struct.*, **73**, 229-241. https://doi.org/10.1016/j.tws.2013.08.007.

Saberi, S., Memarzadeh, P. and Zirakian, T. (2019), "Study of buckling stability of cracked plates under uniaxial compression using singular FEM", *Struct. Eng. Mech.*, **69**(4), 417-426. https://doi.org/10.12989/sem.2019.69.4.417.

Seifi, R. and Kabiri, A.L. (2013), "Lateral load effects on buckling of cracked plates under tensile loading", *Thin-Wall. Struct.*, **72**, 37-47. https://doi.org/10.1016/j.tws.2013.06.010.

Seif, A.E. and Kabir, M.Z. (2017), "Experimental study on the fracture capacity and fatigue life reduction of the tensioned cracked plate due to the local buckling", *Eng. Fract. Mech.*, **175**, 168-183. https://doi.org/10.1016/j.engfracmech.2017.01.023.

Serror, M.H., Hamed, A.N. and Mourad, S.A. (2016), "Numerical study on buckling of steel web plates with openings", *Steel Compos. Struct.*, **22**(6), 1417-1443. https://doi.org/10.12989/scs.2016.22.6.1417.

Shaw, D. and Haung, Y.H. (1990), "Buckling behavior of a central cracked thin plate under tension", *Fracture Mech.*, **35**(6), 1019-1027. https://doi.org/10.1016/0013-7944(90)90129-5.

Timoshenko, S.P. and Gere, J.M. (1961), Theory of Elastic Stability, (2nd Ed.), McGraw-Hill Book Companies Publishing, New York, USA.

Williams, M.L. (1957), "On the stress distribution at the base of a stationary crack", *Journal of Applied Mechanics*, **24**, 109-114.

Yin, S., Yu, T. and Bui, T.Q. (2016), "Buckling and vibration extended isogeometric analysis of imperfect graded Reissner-Mindlin plates with internal defects using NURBS and level sets", *Comput. Struct.*, **177**, 23-38. https://doi.org/10.1016/j.compstruc.2016.08.005.

Yu, T., Bui, T.Q., Yin, S., Doan, D.H., Wu, C.T., VanDo, T. and Tanaka, S. (2016), "On the thermal buckling analysis of functionally graded plates with internal defects using extended isogeometric analysis", *Compos. Struct.*, **136**, 684-695. https://doi.org/10.1016/j.compstruct.2015.11.002.

Zakeri, M., Mozaffari A. and Katirae, M.A. (2018), "Influence of stiffener edge on the buckling load of holed composite plates", *Steel Compos. Struct.*, **29**(5), 681-688. https://doi.org/10.12989/scs.2018.29.5.681.

CC

Nomenclature

a	Crack length
$E,\ \nu$	Material plate modulus of elasticity and Poisson's ratio
$e_x = \frac{x_c}{W/2},\ e_y = \frac{y_c}{L/2}$	Eccentricity ratio in the axis direction x and y
F, G, R	In-plane, out-of-plane and rotation enrichment functions
F_{col}	Fracture collapse function
H	Heaviside function
K_I	Mode I stress intensity factor
K_{IC}	Critical value of the mode I stress intensity factor
k_{cr}	Buckling coefficient
L, W, t	Plate length, width and thickness
N	Conventional shape functions
u, v, w	Displacement components in x, y and z directions
$x_c,\ y_c$	Eccentricity of the crack in the axis direction x and y
λ_T	Buckling multiplier in tension
σ_T	Buckling stress in tension
σ_E	Euler buckling stress in compression for un-cracked plate
φ	Dimensionless stress intensity factor
β	Fracture toughness parameter
$\boldsymbol{\varepsilon}^L,\ \boldsymbol{\varepsilon}^{NL}$	Linear and non-linear strain vectors
$\mathbf{D}$	Tensor of material properties
$\hat{\mathbf{S}}$	Initial stress vector
$\mathbf{S}$	Stress matrix
$\mathbf{K}_S,\ \mathbf{K}_G$	Standard and geometric stiffness matrices
$\mathbf{B}_S,\ \mathbf{B}_G$	Standard and geometric strain-displacement matrices